Department of Electronics and Nanoengineering

Transient Nonlinear Optics of Two-Dimensional Materials

Yadong Wang

Aalto University

DOCTORAL THESES

Aalto University publication series
DOCTORAL THESES 31/2022

Transient Nonlinear Optics of Two-Dimensional Materials

Yadong Wang

A doctoral thesis completed for the degree of Doctor of Science (Technology) to be defended, with the permission of the Aalto University School of Electrical Engineering, Remote Zoom meeting, on 4th March 2022.

Aalto University
School of Electrical Engineering
Department of Electronics and Nanoengineering
Photonics Group

Supervising professor
Professor Zhipei Sun, Aalto University, Finland

Preliminary examiners
Associate Professor Alexander Solntsev, University of Technology Sydney, Australia;
Professor Wenshan Cai, Georgia Institute of Technology, United States of America.

Opponent
Professor Nathalie Vermeulen, Vrije Universiteit Brussel, Belgium

Aalto University publication series
DOCTORAL THESES 31/2022

ISBN 978-952-64-0714-2 (printed)
ISBN 978-952-64-0715-9 (pdf)
ISSN 1799-4934 (printed)
ISSN 1799-4942 (pdf)
http://urn.fi/URN:ISBN:978-952-64-0715-9

Unigrafia Oy
Helsinki 2022

Finland

Printed matter
4041-0619

Author
Yadong Wang

Name of the doctoral thesis
Transient Nonlinear Optics of Two-Dimensional Materials

Publisher School of Electrical Engineering

Unit Department of Electronics and Nanoengineering

Series Aalto University publication series DOCTORAL THESES 31/2022

Field of research Advanced Materials and Photonics

Manuscript submitted 7 September 2021 **Date of the defence** 4 March 2022

Permission for public defence granted (date) 14 January 2022 **Language** English

☐ **Monograph** ☒ **Article thesis** ☐ **Essay thesis**

Abstract

Two-dimensional (2D) layered materials with remarkable optical and electronic properties, are promising for a variety of applications in the area of electronics, photonics, and optoelectronics. Recently, increasing efforts are targeted toward the nonlinear optical properties of 2D materials, which are not only fascinating in terms of fundamental physics, but also intriguing for various potential applications. Beneficial from their atomically thin nature, 2D materials are the ideal material to address the subjects on how the materials respond to the light excitation without considering phase-matching effects.

In this thesis, I devote main efforts to studying the relation between carrier dynamics and nonlinear optical responses in 2D materials and to developing potential applications in the area of ultrafast nonlinear optics. Details are expressed as below:

1. Transient linear optical absorption of monolayer MoS2 is studied in the sub-bandgap region from 860 nm to 1400 nm. A significant absorption enhancement of up to 4.2% is observed due to the pump-induced absorption at the excited carrier states.

2. Transient second-harmonic generations in transition metal dichalcogenide monolayers are investigated in a broadband energy range. The pump modified excitonic oscillation strength enables to enhance the SHG at dark exciton states and bleach the SHG at bright exciton states. The enhancement of SHG is achieved as high as 386 times. Further, the SHG modulation has been realized with a modulation depth of up to 60% and a response time of ~600 fs.

3. Transient higher-order harmonic generations are finally studied. Broadband third-harmonic spectroscopy displays a series of electronic states in monolayer MoS2 with high signal contrast up to 800 times. The ultrafast photocarrier dynamics of electronic states in MoS2 are explored by transient third-harmonic generation. Further, the all-optical modulation of high-harmonic generation in monolayer MoS2 is demonstrated with a modulation depth up to 90%, offering a promising platform for the ultrafast optical signal processing of nonlinear optics.

Keywords Nonlinear Optics, Two-Dimensional Materials, Pump-Probe Spectroscopy, Excitonic States, Harmonic Generations, Ultrafast All-Optical Modulation

ISBN (printed) 978-952-64-0714-2 **ISBN (pdf)** 978-952-64-0715-9

ISSN (printed) 1799-4934 **ISSN (pdf)** 1799-4942

Location of publisher Helsinki **Location of printing** Helsinki **Year** 2022

Pages 190 **urn** http://urn.fi/URN:ISBN:978-952-64-0715-9

Acknowledgements

This research work has been carried out in the Photonics group at the Department of Electronics and Nanoengineering, Aalto University, Finland. First of all, I would like to express my deepest appreciation to my supervisor and advisor, Professor Zhipei Sun and thank him for giving me this opportunity to surf in this research ocean. His world-class expertise in the field of photonics has been a great source of learning and professional inspiration for me and will last during my future career life. I feel privileged in having him as my supervisor and he has been proved as an invaluable mentor throughout my research work. My gratitude also goes to my previous supervisor Prof. Jianlin Zhao and Prof. Xuetao Gan. Without their supports, this research cannot be carried out.

Also, I would like to thank Prof. Masood Ghotbi for his guidance about the basic technical issues of nonlinear optics. I am very appreciated to have hundreds of discussions with Dr. Yunyun Dai and Dr. Susobhan Das during these years, which stimulated lots of ideas as well as happy moments. The way they understand fundamental physics and solve problems often inspired me to think more and broadly. Besides, I would like to thank Dr. He Yang, Dr. Anton Autere, Dr. Hui Xue, Dr. Henri Jussila, Dr. Diao Li, Dr. Mei Qi for their great help at my starting time in Finland. I wish to express my appreciation to all my former and present colleagues as well as the department staffs for providing an amazing working environment. I thank the people working at Micronova for their constructive and valuable comments on our research work. Special thank to Dr. Mingde Du for the help to advise this thesis.

In addition, I express my deep thank to all our collaborators: Especially for theoretical calculations, Prof. F. Javier García de Abajo and Dr. Fadil Iyikanat from ICFO-Institut de Ciencies Fotoniques, Prof. Habib Rostami from Nordita and Stockholm University. Lots of discussions for the theoretical understanding of fundamental physics have largely broadened my horizontal knowledge. I also thank Dr. Shisheng Li for providing samples of two-dimensional materials. We cannot carry on our ideas without these samples.

This work has been financed by Aalto Centre for Quantum Engineering, Academy of Finland, Academy of Finland Flagship Programme. The research grants awarded by China Scholarship Council, Finnish Foundation for Technology Promotion, Foundation for Aalto University Science and Technology are gratefully acknowledged. The Nanofabrication centre at Micronova is highly acknowledged for supporting the research infrastructure.

Besides, I would like to thank my friends for sharing their happiness in Finland. I wish you all with a happy life.

Last but not least, I would like to express my deepest gratitude to my mother and my family for your trust and encouragement. None of this thesis continues without your support. Thank all of you with great wishes! Finally, I wish to give my honest appreciation to my fiancée. Without her, I could not persist in my research.

"It's not enough to read, to listen, to be passive. One must act."
— Adam Weishaupt

Espoo, 26 June 2021
Yadong Wang

Contents

List of Abbreviations and Symbols

A	Absorptivity
CVD	Chemical vapor deposition
DFG	Difference-frequency generation
DM	Dichroic mirror
EOM	Electro-optic modulator
FWM	Four-wave mixing
GEOM	Graphene electro-optic modulator
h-BN	Hexagonal boron nitride
HHG	High-harmonic generation
LED	Light-emitting devices
ME	Mechanical exfoliation
NLO	Nonlinear optical
NRZ	Non-return-to-zero
OC	Optical fiber coupler
OPA	Optical parametric amplification
OPO	Optical parametric oscillation
OSC	Oscilloscope
PD	Photodetector
PMT	Photomultiplier tube
SA	Saturable absorption
SEM	Scanning electron microscopy
SFG	Sum-frequency generation
SHG	Second-harmonic generation
TA	Transient absorption

TFBG	Tilted fiber Bragg grating
THG	Third-harmonic generation
TMD	Transition metal dichalcogenides
WDM	Wavelength division multiplexing
2DM	Two-dimensional materials
$\chi^{(2)}$	Second-order nonlinear susceptibility
$\chi^{(3)}$	Third-order nonlinear susceptibility
$\chi^{(n)}$	n-order nonlinear susceptibility
E_F	Fermi level
σ+	Left-circular polarized
σ-	Right-circular polarized
I_{sc}	Short-circuit current
V_{oc}	Open-circuit voltage
ω	Light frequency
Re(x)	Real part of x
Im(x)	Imaginary part of x

List of Publications

This doctoral dissertation consists of a summary and of the following publications which are referred to in the text by their numerals

1. Yadong Wang, Masood Ghotbi, Susobhan Das, Yunyun Dai, Shisheng Li, Xuerong Hu, Xuetao Gan, Jianlin Zhao, and Zhipei Sun, Difference frequency generation in monolayer MoS_2. Nanoscale, 12 (38), 19638 (2020).

2. Yadong Wang, Biqiang Jiang, Susobhan Das, Qiang Zhao, Xuetao Gan, and Jianlin Zhao, All-optically controlled slow and fast lights in graphene-coated tilted fiber Bragg grating. Applied Physics Express, 12 (7), 072010 (2019).

3. Yadong Wang, Susobhan Das, Fadil Iyikanat, Yunyun Dai, Shisheng Li, Xiangdong Guo, Xiaoxia Yang, Jinluo Cheng, Xuerong Hu, Masood Ghotbi, Fangwei Ye, Harri Lipsanen, Shiwei Wu, Tawfique Hasan, Xuetao Gan, Kaihui Liu, Dong Sun, Qing Dai, F. Javier García de Abajo, Jianlin Zhao and Zhipei Sun, Giant all-optical modulation of second-harmonic generation mediated by dark excitons. ACS Photonics, 8 (8), 2320 (2021).

4. Yadong Wang, Fadil Iyikanat, Habib Rostami, Xueyin Bai, Xuerong Hu, Susobhan Das, Yunyun Dai, Luojun Du, Yi Zhang, Shisheng Li, Harri Lipsanen, F. Javier García de Abajo, and Zhipei Sun, Probing Electronic States in Monolayer Semiconductors through Static and Transient Third-Harmonic Spectroscopies. Advanced Materials, 2107104 (2021).

5. Jakub Bogusławski†, **Yadong Wang**†, Hui Xue, Xiaoxia Yang, Dong Mao, Xuetao Gan, Zhaoyu Ren, Jianlin Zhao, Qing Dai, Grzegorz Soboń, Jarosław Sotor, and Zhipei Sun, Graphene actively mode-locked lasers. Advanced Functional Materials, 28 (28), 1801539 (2018). †**Equal contribution.**

6. Hui Xue†, **Yadong Wang**†, Yunyun Dai, Wonjae Kim, Henri Jussila, Mei Qi, Jannatul Susoma, Zhaoyu Ren, Qing Dai, Jianlin Zhao, Kari Holonen, Harri Lipsanen, Xiaomu Wang, Xuetao Gan, and Zhipei Sun, A $MoSe_2/WSe_2$ heterojunction-based photodetector at telecommunication wavelengths. Advanced Functional Materials, 28 (47), 1804388 (2018). †**Equal contribution.**

7. Susobhan Das, **Yadong Wang**, Yunyun Dai, Shisheng Li, and Zhipei Sun, Ultrafast transient sub-bandgap absorption of monolayer MoS_2. Light: Science & Applications, 10 (1), 27 (2021).

8. Yunyun Dai, **Yadong Wang**, Susohban Das, Hui Xue, Xueyin Bai, Eero Hulkko, Guangyu Zhang, Xiaoxia Yang, Qing Dai, and Zhipei Sun, Electrical Control of Interband Resonant Nonlinear Optics in Monolayer MoS_2. ACS Nano, 14 (7), 8442 (2020).

9. Yunyun Dai, **Yadong Wang**, Susobhan Das, Shisheng Li, Hui Xue, Ahmadi Mohsen, and Zhipei Sun, Broadband Plasmon-Enhanced Four-Wave Mixing in Monolayer MoS_2. Nano Letters, 21 (14), 6321 (2021).

10. Anton Autere, Henri Jussila, Yunyun Dai, **Yadong Wang**, Harri Lipsanen, and Zhipei Sun, Nonlinear optics with 2D layered materials. Advanced Materials 30 (24), 1705963 (2018).

11. Diao Li, Hui Xue, **Yadong Wang**, Mei Qi, Wonjae Kim, Changfeng Li, Juha Riikonen, Zhaoyu Ren, Jintao Bai, Harri Lipsanen, and Zhipei Sun, Active synchronization and modulation of fiber lasers with a graphene electro-optic modulator. Optics Letters 43 (15), 3497 (2018).

12. Diao Li, Hui Xue, Mei Qi, **Yadong Wang**, Sinan Aksimsek, Nikolai Chekurov, Wonjae Kim, Changfeng Li, Juha Riikonen, Fangwei Ye, Qing Dai, Zhaoyu Ren, Jintao Bai, Tawfique Hasan, Harri Lipsanen, and Zhipei Sun, Graphene actively Q-switched lasers. 2D Materials 4 (2), 025095 (2017).

Author's Contribution

Publication 1: Difference frequency generation in monolayer MoS_2

The author performed all the major experiments except the polarization dependent measurement. Co-authors fabricated the samples and performed the corroborative polarization measurement.

Publication 2: All-optically controlled slow and fast lights in graphene-coated tilted fiber Bragg grating

The author prepared the sample, conducted all the major experiments with collaborators, analysed the data, and wrote the manuscript together with the co-authors.

Publication 3: Giant all-optical modulation of second-harmonic generation mediated by dark excitons

The author conceived the idea, performed all the major experiments (except the power dependent modulation part) and wrote the manuscript. Co-authors fabricated the samples and theoretically analysed the data and optimized the manuscript.

Publication 4: Probing electronic states in monolayer semiconductors with third-harmonic spectroscopies

The author conceived the idea, conducted all the major experiments (except the sample characterization part), wrote the manuscript together with the co-authors. Co-authors grew the samples and theoretically analysed the data and optimized the manuscript.

Publication 5: Graphene actively mode-locked lasers

The author performed the modulator measurements and laser system characterizations, and wrote the modulator part of the manuscript.

Publication 6: A $MoSe_2/WSe_2$ heterojunction-based photodetector at telecommunication wavelengths.

The author set up the photocurrent measurement system and laser source at telecommunication band, took part in writing the manuscript.

Publication 7: Ultrafast transient sub-bandgap absorption of monolayer MoS_2.

The author set up the transient absorption experimental system, analysed the data, took part in writing the manuscript.

Publication 8: Electrical control of interband resonant nonlinear optics in monolayer MoS_2.

The author set up the four-wave mixing experimental system, took part in writing the manuscript.

Publication 9: Broadband Plasmon-Enhanced Four-Wave Mixing in Monolayer MoS_2.

The author set up the four-wave mixing experimental system, took part in writing the manuscript.

Publication 10: Nonlinear optics with 2D layered materials

The author wrote the saturable absorption section of the manuscript and prepared Figures 2, 3, 5, 11, organized the references and took part in writing the manuscript.

Publication 11: Active synchronization and modulation of fiber lasers with a graphene electro-optic modulator

The author assisted the experimental measurements, and took part in writing the manuscript.

Publication 12: Graphene actively Q-switched lasers

The author assisted the experimental measurement, and took part in writing the manuscript.

1. Introduction

Nonlinear optics is the branch of optics that examines the light behaviour in nonlinear optical media, which plays an increasingly important role in various technologies in our modern information society. Harmonic generations (HGs) are a series of nonlinear optical processes, in which incident photons generate new photons with harmonic frequencies of the incident photons. As the most widely used nonlinear optical effects, second-harmonic generation (SHG), originating from second-order nonlinear optical susceptibility $\chi^{(2)}$ mainly in noncentro-symmetric materials, was first reported in 1961 immediately after the invention of the laser.[1] It is normally regarded as one of the most efficient nonlinear optical processes and has been widely exploited for various important applications, such as coherent light generation [2], crystalline characterization [3], bioimaging [4], and spectroscopy [5]. In addition, the third-harmonic generation (THG) with third-order nonlinear optical susceptibility $\chi^{(3)}$ is also primarily useful for many applications.[6] Different from SHG, THG could occur in the materials without considering symmetry breaking. THG can also be directly dependent on one-, two-, and three-photon transition resonances with electronic states, which gives additional freedom of 3-photon resonance than that of SHG.[6] Further, the development of high-harmonic generation (HHG) has also played a basis for attosecond science.[7] Normally, nonlinear optical processes have relatively low efficiency. And high-order harmonic generation requires higher intense incident light due to the relatively low higher-order nonlinear susceptibility. Therefore, reinforcing the conversion efficiency of HGs is of significant importance for numerous applications of nonlinear optics.

There are many approaches to enhance the conversion efficiency of nonlinear optics, such as employing materials with high nonlinear optical susceptibility, increasing the light-matter interaction length and optimizing phase matching condition. Currently, the commercial nonlinear optical materials are mainly bulk crystals, such as potassium titanyl phosphate (KTP), beta barium borate (BBO), and lithium iodate ($LiIO_3$). They have enabled the great success of nonlinear optics in practical applications. While the emerging and future technology typically demands miniaturization of the photonic and optoelectronic devices for on-chip integration. To achieve this objective, on-chip nonlinear photonic devices have been demonstrated by using highly confined electromagnetic fields (such as, high *Q*-factor resonators or plasmonic resonances). It offers one possible way for enhancement of nonlinear optics, while the nonlinear optical susceptibility itself is low but with high loss, which drives scientists to search for

novel materials with strong nonlinear optical susceptibility (such as low-dimensional materials).

In addition to optical nonlinearity enhancement, active control of nonlinear optical processes is desirable for practical applications, in analogy to the linear active optical devices. In particular, it is extremely fascinating to all-optically modulate nonlinear optical responses of materials with high efficiency and ultrafast speed, for a large range of applications [8], such as optical data processing, optical communications[9], optical frequency comb generation, and quantum optics [10]. However, the active control of traditional bulk materials is distressful due to their slow speed or less efficiency. To address these challenges, thin films have been first employed (such as metals [11] and semiconductors [12],) but their performance on nonlinear optical modulation is generally very weak (typically with enhancement factors of < 2 [13-15]). The efficient all-optical modulation strategies to control nonlinear optical processes still have remained elusive.

The recent discovery and development of two-dimensional (2D) materials offer a promising platform for actively engineered nonlinear optics. Indeed, 2D materials such as graphene, transition metal dichalcogenides (TMDs) have attracted huge interest in the field of photonics and optoelectronics.[16,17] The 2D structure naturally confines the electrons into the atomic level, which gives an opportunity to form a strong light interaction. For example, graphene with 0.3 nm thickness has as high as 2.3% broadband linear optical absorption [18] and the nonlinear optical susceptibility up to $\chi^{(3)} \sim 10^{-7}$ esu [19] due to the resonance in the linear-dispersion band structure. On the other hand, with the extreme quantum confinement and reduced screening effect, monolayer TMDs have significant excitonic quasi-particles induced resonance, which prominently dominates their linear and nonlinear optical properties.[20-25] Further, 2D materials with atomic thickness naturally have large mechanical deformation and flexible structure, which can be easily integrated with other devices, such as on-chip waveguides without considering lattice matching. It thus holds great promises for future integrated devices both in optoelectronics and photonics.[26,27] However, the conversion efficiency in 2D materials remains relatively low with the atomic thickness, comparing to bulk materials, which hinders their potential applications.

This thesis aims to study the transient linear and nonlinear optical processes in different 2D materials, and demonstrate new methods to control and enhance their nonlinear optical responses, specifically SHG, THG, HHG. More specifically, the key objectives of this thesis are described as follows:

1. Transient linear optical absorption in the transparent region of monolayer MoS_2: The ultrafast transient optical absorption of monolayer MoS_2 is investigated in the sub-bandgap region from 860 nm to 1400 nm. A significant absorption enhancement of up to 4.2% is observed due to the pump-induced re-absorption at the excited carrier states.
2. SHG modulation in TMD monolayers: A giant and broadband all-optical ultrafast modulation of SHG in TMD monolayers has been investigated. The pump modified excitonic oscillation strength enables to enhance the

SHG at dark exciton states and bleach the SHG at bright exciton states. The enhancement of SHG has been achieved as high as 386 times, two orders of magnitude larger than previous results. Further, the SHG modulation has been realized with a modulation depth of up to 60% and response time of < 600 fs.

3. Probing Rydberg states of excitons in 2D transition TMDs with THG spectroscopies: Series of electronic states in monolayer MoS_2, such as multiple excitonic Rydberg states and free-particle energy bands, have been explored, with significant contrast of up to 800 times via broadband (from ~1.77 to 3.10 eV) third-harmonic spectroscopy. Further, the photocarrier dynamics of electronic states in MoS_2 have been explored by transient THG, giving direct evidence of various carrier relaxation processes, such as exciton formation and electron-phonon interaction.
4. Optical control of HHG in 2D TMDs: The all-optical modulation of HHG in monolayer MoS_2 has been demonstrated with the assistance of the modified interlayer transitions. Thanks to the strong resonance oscillation of excitons in monolayer MoS_2, the HHG is largely modulated with a modulation depth of 90% by a pump light at a wavelength of 400 nm.

This thesis is arranged as follows: After chapter 1 (this chapter), it begins by presenting the fundamentals of 2D materials and related electrical, optical properties in chapter 2. The fundamental of nonlinear optics and the current state-of-the-art nonlinear optics with 2D materials are detailly discussed in chapter 3. Chapters 4-6 introduce the transient linear, SHG, THG, HHG in 2D materials, respectively. Finally, chapter 7 summarizes this thesis and presents a perspective outlook of the above results from the fundamental and technological points of view.

2. Fundamentals of 2D materials

Two-dimensional materials (2D materials), are the natural layered materials with a thickness on the atomic scale and normally with a much large surface area (≥μm), where electrons in these materials are confined to move within the two-dimensional plane. Graphene with a single sheet of carbon atoms is discovered as the first 2D material in 2004, which broke the argument about the non-existence of strictly 2D crystalline materials.[28] Since then, hundreds of 2D materials, such as transition metal dichalcogenides (TMDs), phosphorene, hexagonal boron nitride (h-BN), Xenes, have been fabricated with various methods (such as mechanical exfoliation (ME), liquid exfoliation, and chemical vapor deposition (CVD)). With isolation into single or few-layer from bulk materials, 2D materials exhibit remarkable physical and chemical properties [28] mainly due to: i) removal of van der Waals interactions, ii) an increase in the ratio of surface-area-to-volume, iii) confinement of electrons in an atomic plane. Such properties could be employed for vast promising applications [29], such as transistors[30], ultrafast lasers [31], photodetectors [32], valleytronics [33]. This chapter will give a brief introduction to optical and electrical properties of 2D materials, specifically graphene and monolayer TMDs.

2.1 Graphene

2.1.1 Electrical and optical properties

Graphene is a single carbon layer, in which each carbon atom is covalently sp^2 hybridized bonding with three other carbon atoms in an arrangement of a honeycomb lattice. In graphene, the conduction and valence bands meet at the **K** point (i.e. Dirac points) of the Brillouin zone, as shown in Figure 2.1(a).[34] Therefore, graphene is regarded as a semimetal. And the electron band in graphene obeys a linear dispersion relation of $E=\upsilon_F hk$, where $\upsilon_F = 10^6$ m/s is the Fermi velocity, h is the Planck constant, k is the wave vector. This unique band structure enables distinctive electronic properties. Figure 2.1(b) shows the evolution of graphene's conductivity (σ) as a function of gate voltage[35], which increases linearly with the substantial electron (hole) doping. The linear dependence of conductivity gives the carrier mobilities $\mu=\sigma/ne$ as high as 200000 cm^2/Vs, where n is the concentration of electrons or holes and e is the electron charge.[36] This high carrier mobility is promising for ultrafast electronics [37],

including digital logic, high-frequency transistor, circuits (e.g., mixers and radio-frequency amplifiers).

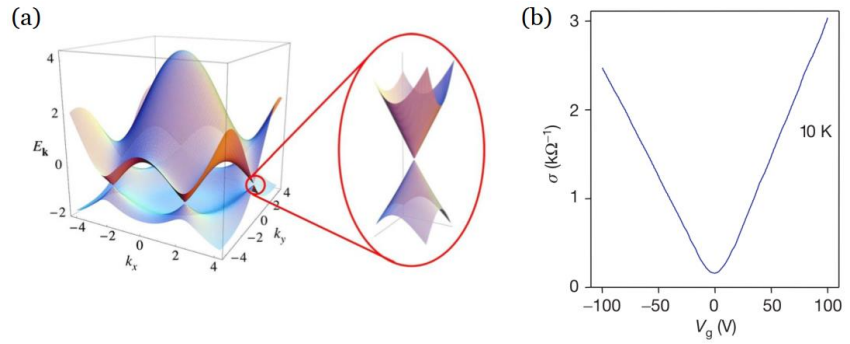

Figure 2.1. (a) Electronic band structures of graphene.[34] (b) Changes of graphene's conductivity as a function of gate voltage V_g.[35]

Due to the linear dispersion of the massless Dirac fermions, the optical conductivity of graphene in the near-IR and visible regions has a universal value.[18] The absorption of graphene within this broadband frequency region is around 2.3%. Thus, it can be even observed under optical microscopy with naked eyes after contrast engineering. If considering the 0.334-nm thickness of graphene, the absorption coefficient in graphene is ~7×10^7 m^{-1}, which is ~50 times higher than that of GaAs at the telecommunication band.[38] While the absorption index of graphene at higher energy (normally > 3 eV) shows the deviated value with the universal one due to many-body effects.[39] Excitingly, the optical responses in graphene are highly dependent on the relation of optical energy and Fermi level, owing to Pauli blocking effect. The interband transitions are essentially blocked when photon energies $\omega < 2|E_F|$, where E_F is the Fermi level. The E_F in graphene can be adjusted with chemical or physical doping, enabling actively tunable optics with graphene. Figure 2.2 shows the optical transmission of our homemade graphene device at the photon energy of 0.8 eV with the relation of gate voltage.[40] Another exciting property of graphene is ultrafast carrier dynamics, where the carriers in the excited state decay and recombine very fast within several picoseconds, much faster than the bulk materials (normally as hundreds of picoseconds to nanoseconds).[41] Such ultrafast carrier interaction is crucial to ultrafast optoelectronic applications.[42]

Besides the linear optical properties, the nonlinear optical responses of graphene have been found with remarkable strong and broadband features. By comparing with a thin gold layer, the third-order optical susceptibility is obtained as $\chi^{(3)} \sim 10^{-7}$ esu [19], which is 8 orders of magnitude larger than that in transparent dielectric materials. Thus far, the nonlinear optical properties of graphene such as broadband saturable absorption [31], photothermal effect [26,27,43], third-harmonic generation [44-46], four-wave mixing [19,47], self-phase modulations [48-50], high-harmonic generation [51,52], optical limiting [53] and nonlinear Kerr effect [54-56] have been widely investigated. Although graphene has a centrosymmetric structure, the second-harmonic generation has

been found from the interface with a substrate or from quadrupole response.[57,58] Meanwhile, the inversion symmetry can be broken by many methods such as electrical gating [59-61], chemical etching [62]. Similar to the linear response, nonlinear optical responses in graphene are sensitive to carrier doping, which gives an opportunity for tunable nonlinear optics.[63-66]

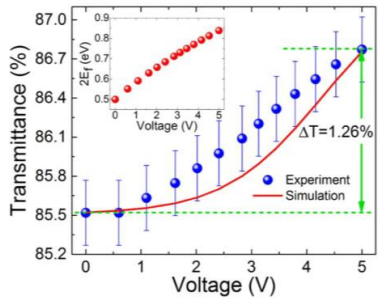

Figure 2.2. Gate tunable optical transmittance of graphene at the photon energy of 0.8 eV, where blue dots are experimental results and red curve is theoretical calculation. Inset curve is the calculated Fermi energy as a function of the gate voltage. Adapted from Publication 12.

2.1.2 Photonic and optoelectronic applications

The richness of optical and electronic properties of graphene gives rise of potential applications in photonics and optoelectronics, ranging from solar cells and light-emitting devices to touch screens, photodetectors, and ultrafast lasers.[67] For instance, the broadband absorption in monolayer graphene makes it a promising material for broadband optical devices (e.g., wideband photodetectors [29,67], saturable absorbers [67-69], and modulators [70]), covering an extremely wide spectral range from the ultraviolet to microwave regions. Here, two examples of graphene's applications are introduced: actively modulated pulsed lasers, and optically controlled slow and fast light.

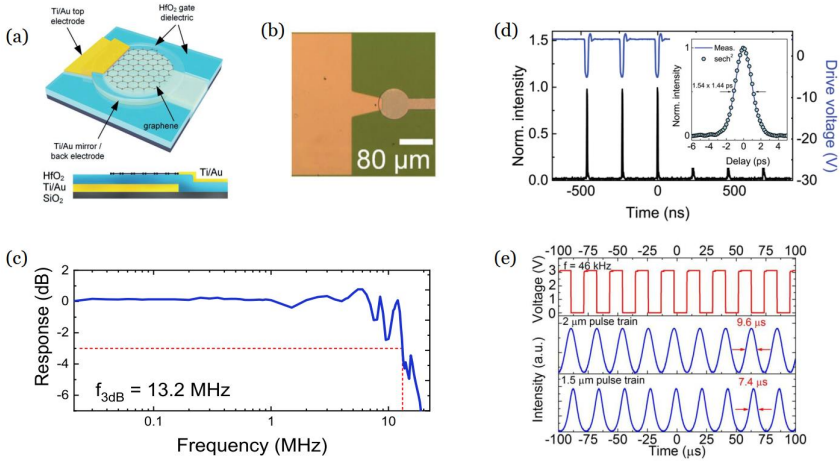

Figure 2.3. Graphene electro-optic modulators and pulsed laser generations. (a) Schematic illustration (up) and cross-section (down) of a graphene modulator. (b) Optical image of fabricated

GEOM device. (c) Operation of frequency bandwidth at 1550 nm. (d) Actively mode-locked laser pulse train synchronized with modulation voltage. Inset, autocorrelation trace of the output pulses. (e) The modulated signal (top panel) and synchronously *Q*-switched laser pulse trains at 2 μm (middle panel) and 1.5 μm (bottom panel). Figure (a)-(d) are adapted from Publication 5, Figure (e) is adapted from Publication 11.

Generally, pulsed lasers are vital for widespread applications in various fields such as spectroscopy, materials processing, and digital telecommunications [71], which can be implemented with either active or passive methods. With the active method, the optical modulator is inserted into the laser cavity to actively switch the loss of intra-cavity light, while the passive one typically relies on saturable absorbers (SAs) by introducing all-optical self-modulation effect.[31] In comparison to the passive one, the active method allows more freedoms for electrically tunable laser parameters, such as repetition rate, pulse duration, and energy, which is favourable for applications. Graphene electro-optic modulators (GEOMs) have been demonstrated to achieve actively modulated pulsed lasers. An example of the GEOM is shown in Figure 2.3. The modulator consists of metal contacts, an insulator layer, and monolayer graphene. Figure 2.3(a) and (b) give the schematic illustration and optical image of GEOM, respectively. The diameter of GEOM is around 80 μm to fit the diameter size of the laser spot. Besides the optical tunable absorption of GEOM, the other key parameter is the operation bandwidth for the modulator. Figure 2.3(c) shows the dynamic electro-optical response of a free-space GEOM device, which exhibits a flat response with a 3-dB bandwidth of ~13.2 MHz. By employing the GEOM, actively *Q*-switched (1550 nm and 2000 nm [40]) and mode-locked (1550 nm in Figure 2.3(d) [72]) have been demonstrated. The broadband operation of GEOM allows another important application: actively synchronized pulsed lasers (e.g., 1550 nm and 2000 nm laser synchronization in Figure 2.3(e) [73]).

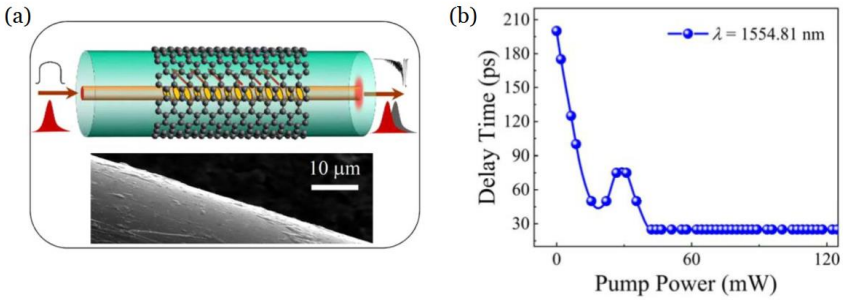

Figure 2.4. Graphene based tunable TFBG. (a) Schematic diagram of the graphene coated TFBG. (b) SEM Image of the graphene coated TFBG. (b) Delay times of signal pulses at the wavelength of 1554.81 nm as a function of pump power. Adapted from Publication 2.

On the other hand, graphene has been employed as an effective media to delay or accelerate light pulses, which is promising in the area of signal processing and optical communication networks.[74] Figure 2.4(a) shows the schematic diagram of a 6° slanted tilted fiber Bragg grating (TFBG) coated by few-layered graphene. The scanning electron microscopy (SEM) image further confirms the tight joint between graphene and TFBG. By employing graphene's photothermal effect, the refractive index of TFBG is changed with pump light excitation. Thus,

the group delay of the graphene-coated TFBG (GTFBG) can be well controlled by a pump light. Figure 2.4(b) shows the delay time of the signal as a function as pump power, which have been achieved as large as 200 ps and enable to be tuned continuously. This simple, broad-bandwidth, compact approach to actively control the slow and fast light offers potential applications for tunable optical data synchronizations and optical memories. Similar design with optical properties of graphene could also be promising for other platforms such as an on-chip scheme for active optical devices.[75]

2.2 Transition metal dichalcogenide monolayers

2.2.1 Electrical and optical properties

In contrast to the zero bandgap of graphene, transition metal dichalcogenides (TMDs), MX_2 (M = Mo, W; X_2 = S, Se) are typically semiconductors with bandgaps ranging from near-infrared to the visible region. As shown in Figure 2.5(a), TMDs consist of a single layer of transition metal atoms sandwiched by two layers of chalcogen atoms with the trigonal prismatic structure. In the out-plane, they have mirror symmetry, while in-plane inversion symmetry is broken. Limiting to the monolayer, these materials become direct bandgap semiconductors at the K and K' points.[17,24] This is due to the increased indirect-gap value with the strong quantum confinement effect in the out-of-plane direction, while the direct gap at the K (K') point remains mostly unchanged.[76] The electronic bands of TMD monolayers can be calculated (e.g., the GW-BSE method), yielding reliable predictions for the exciton properties of ultra-thin transition metal dichalcogenides.[77,78] Figure 2.5(b) shows the electronic band structure calculated within the GGA and G_0W_0 approximations for monolayer MoS_2.

Compared with graphene, the spin-orbit interaction in TMDs is much stronger mainly originated from their relatively heavy elements and the involvement of the transition metal *d* orbitals. In TMD monolayers, the spin splitting at the K (K') point in the valence band is found ~0.2 eV (Mo) and ~0.4 eV (W).[79,80] This coupling leads to the two valence sub-bands, corresponding to two types of excitons, A and B. With D_{3h} point symmetry, optically generated electrons and holes are both valley and spin polarized. Therefore, with the circular-polarized excitation, the exciton emission in TMD monolayers can be co-polarized followed by the selection rule.[24]

Due to the weak dielectric screening and strong confinement, TMD monolayers give rise to an extraordinarily strong Coulomb interaction, which leads to various fascinating many-particle phenomena. For example, the formation of different types of excitons: neutral exciton, trion, biexciton formed, as well as interlayer exciton states from with different layers.[24,81] The excitons in TMD monolayers exhibit binding energies ~0.5 eV which is one to two orders of magnitude larger than in conventional bulk materials, such as GaAs.[82] Therefore, excitonic features are stable at room temperature and dominate the optical responses of these materials. As shown in the upper panel of Figure 2.5(c), the

reflectance contrast from monolayer MoS_2 on a sapphire substrate exhibits three prominent peaks at 1.85, 2.00, 2.84 eV in room temperature, corresponding to the well-known $1s_A$, $1s_B$, $1s_C$ excitons, respectively. By mathematically 2nd-derivative of the spectrum, the relatively weak excitons also appear. As shown in the down panel of Figure 2.5(c), the dips at 2.17, 2.38, 3.05 eV, corresponding to the 2*s*, 3*s*, and $1s_D$ exciton states, respectively.[83] It matches well with the absorption calculation with the GW-BSE approach [84], as shown in Figure 2.5(d).

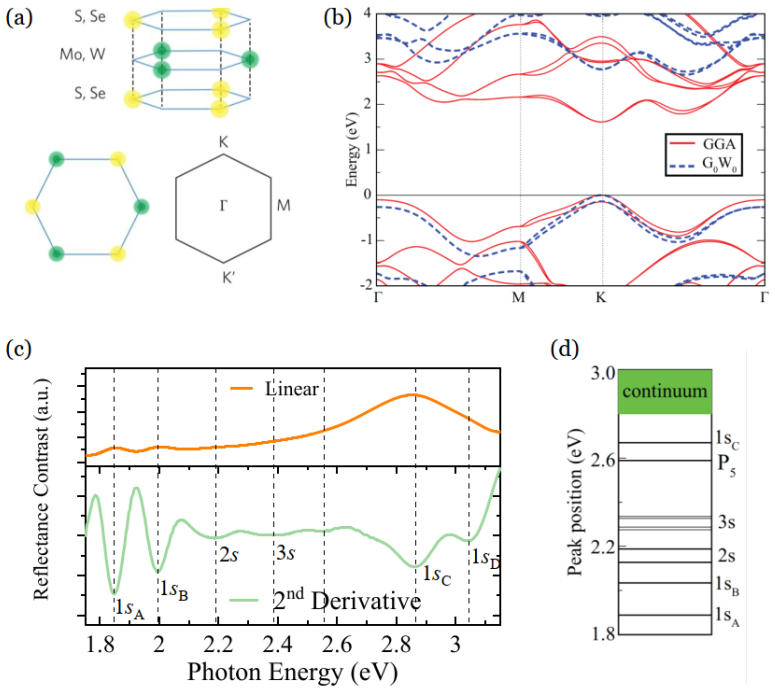

Figure 2.5. (a) Trigonal prismatic structure of monolayer TMDs [17]. (b) Electronic bands of monolayer MoS_2 calculated with the GGA and G_0W_0 approximations. (c) Reflectance contrast in monolayer MoS_2. (d) Calculated absorption states in monolayer MoS_2 within the G_0W_0−BSE approximation. Figure (b-d) are adapted from Publications 3 and 4.

2.2.2 Photonic and optoelectronic applications

With their amazing optical and electrical properties, 2D TMDs are finding various applications for next-generation electronics and optoelectronic devices, especially for photodetectors, light-emitting devices (LEDs), and valleytronics.[17] While graphene-based photodetectors suffer high dark currents due to the semimetal feature of graphene, 2D TMD based photodetectors exhibit lower dark currents and higher responsivity, typically with the operation of photovoltaic effect. Lopez-Sanchez et al. have reported a monolayer MoS_2 photodetector with responsivity as high as 880 A/W.[85] A potentially efficient way is to construct a build-in electric field with a heterostructure. For example, heterostructure devices have been demonstrated for photodetection.[86,87] Figure 2.6(a) shows a heterostructure photodetector with few-layer $MoSe_2$ and WSe_2 on a

280-nm SiO_2/Si substrate. This heterostructure device with a build-in electrical field shows a strong photon response when vias voltage and the gate voltage is zero, as shown in Figure 2.6(b). The maximum photoresponsivity is obtained with 2 A/W at 532 nm with a power of 100 nW, indicating high photodetection performance. Clearly, the heterostructure region reveals pronounced photocurrent generation, exhibiting an attractive platform for the electrical engineered TMD heterostructures for high-performance optoelectronic devices.

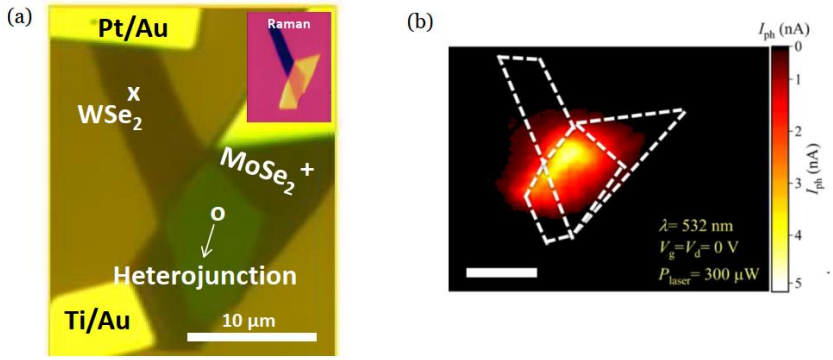

Figure 2.6. The heterostructure photodetector. (a) the optical image of $MoSe_2/WSe_2$ device. Inset: Raman mapping. (b) Photocurrent mapping of the heterostructure. Adapted from Publication 6.

3. Nonlinear optics in 2D materials

Nonlinear optics has grown rapidly with the development of lasers, originating from the study of the interactions of intense light with dielectric media, the applications such as coherent laser sources, material characterizations, and optical signal processing. Along with the long-existing knowledge and techniques of bulk materials, 2D materials have given new insights into nonlinear optics from a fundamental point of view to their potential applications. This chapter gives a brief review of the current state-of-the-art nonlinear optics based on 2D materials.

3.1 Introduction to nonlinear optics

The nonlinear optical effect normally occurs when intense light modifies the optical properties of a material system. And the optical response of the material reacts in a nonlinear manner with the strength of the optical field. To describe this factor, the optical response of materials to the applied electrical field ($\mathbf{E}$) can be expressed by expanding the resulting polarization ($\mathbf{P}$):

$$\mathbf{P}(t) = \varepsilon_0(\chi^{(1)}\mathbf{E}(t) + \chi^{(2)}\mathbf{E}(t)\mathbf{E}(t) + \chi^{(3)}\mathbf{E}(t)\mathbf{E}(t)\mathbf{E}(t) + \cdots) \qquad (3.1)$$

where the coefficients $\chi^{(n)}$ are the n^{th}-order susceptibilities of the material and ε_0 is the vacuum permittivity. The first term $\chi^{(1)}$ is the linear susceptibility with second-rank tensor, which describes the linear optical effects, such as absorption and refraction. The quantities $\chi^{(2)}$ and $\chi^{(3)}$ are known as the second- and third-order nonlinear optical (NLO) susceptibilities, respectively, which are normally weaker than $\chi^{(1)}$. In general, the interaction strength of the nonlinear optical processes typically decreases with a relation of $|\chi^{(n)}|/|\chi^{(n-1)}| \approx 1/|E_0|$, where E_0 is average electrical strength in atom (For example E_0 in a hydrogen atom is ~10^{11} V/m). When the optical field is strong enough, the phenomena caused by higher-order ($n \geq 2$) terms become significant, which could induce new radiation at different frequencies, pulse shaping, or change of refractive index.

The second-order NLO effects, including SHG, difference- and sum-frequency generation (DFG and SFG), the Pockels effect, and optical rectification, are typically induced by the second-order NLO susceptibility $\chi^{(2)}$ in Equation (3.1). The third-order NLO effects, such as THG, four-wave mixing (FWM), optical Kerr effect, and saturable absorption (SA), normally interact with the third-order NLO susceptibility $\chi^{(3)}$ in Equation (3.1). Although higher-order NLO interac-

tions are normally weak, the HHG, multiphoton absorption/scattering/ luminescence with the n^{th}-order NLO susceptibility $\chi^{(n)}$, appears when the laser intensity is extremely high.

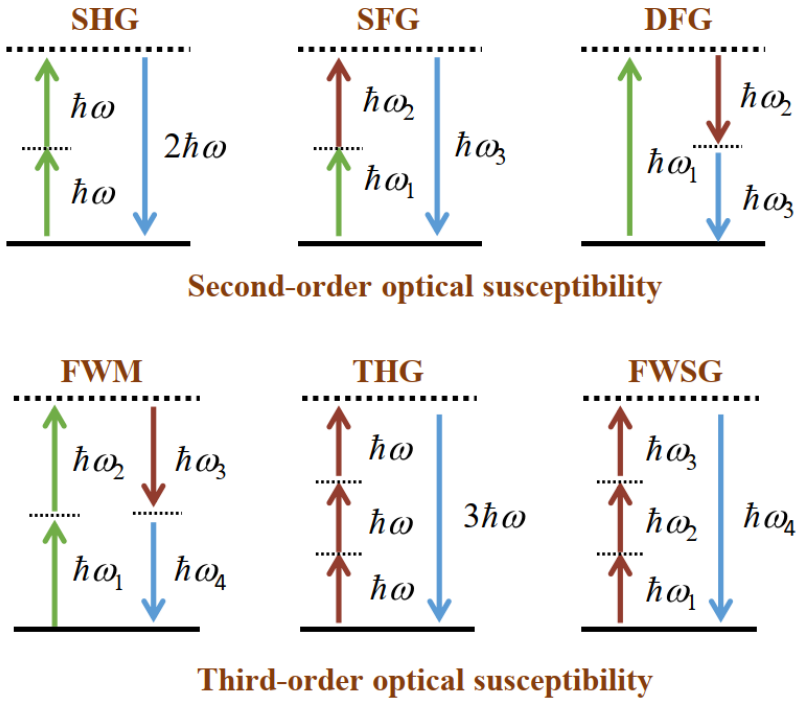

Figure 3.1. Examples of photon diagrams of second- and third-order NLO processes.

Different nonlinear optical processes are commonly explained with photon diagrams, shown in Figure 3.1. In general, harmonic generation is utilized to convert an optical signal to higher frequencies. In SHG (THG), two (three) incident photons at the frequency ω create light radiation at the frequency 2ω (3ω), as shown in Figure 3.1. SHG and THG are the most frequently used nonlinear optical processes for various frequency conversion applications. In SFG, which is analogous to SHG with the difference that the two input photons have different frequencies (i.e., ω_1 and ω_2) and the energy from the ω_1 and ω_2 waves is converted into that at the sum frequency ω_3 (i.e., $\omega_3=\omega_1+\omega_2$). Note that nonlinear processes (in particular various parametric processes, such as SHG, SFG, FWM) are typically phase sensitive, therefore efficient nonlinear frequency conversion requires a proper phase relationship between the interacting waves (i.e., phase-matching). In the case of SHG, perfect phase-matching requires an identical refractive index at different interacting waves (i.e., $n(\omega_1)= n(2\omega_1)$), which is challenging in materials that typically exhibit normal dispersion. To achieve ideal phase-matching, common phase-matching methods involve the use of crystal birefringence and the periodic poling of the crystal. In DFG, the frequency of the generated photon is the difference of the two input frequencies, (i.e., $\omega_3=\omega_1-\omega_2$), shown in Figure 3.1. When two optical waves at frequencies ω_1 and ω_3 interact inside a $\chi^{(2)}$ nonlinear crystal, an additional input light at frequency ω_2 can be

amplified in the DFG process. This is called optical parametric amplification (OPA), which can be utilized to create tunable light amplifiers by mixing the output of two lasers operating at different frequencies. When such an amplification process happens inside an optical resonator, the gain from DFG can produce light oscillation if the gain is larger than cavity loss. These kinds of devices are called optical parametric oscillators (OPO) and they are commonly used to produce wavelength-tunable coherent light (e.g., from the near- to mid-infrared or even terahertz spectral regions). The wavelength tuning in OPOs is achieved by varying the phase-matching condition with the orientation or the temperature of the nonlinear optical crystals. This makes OPOs technologically valuable devices to produce broadband wavelength-tunable light at frequencies that are difficult to achieve with conventional lasers.[88,89]

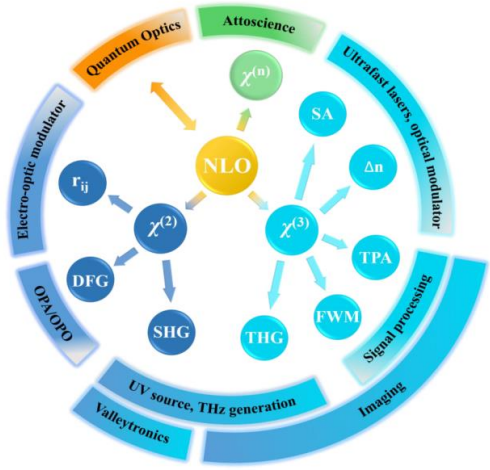

Figure 3.2. Examples of typical NLO applications. TPA: two-photon absorption; r_{ij}: electro-optic coefficient, Δn: intensity dependent refractive index change. Adapted from Publication 10.

Because the input optical field and its dielectric polarization in materials are vector quantities, the nonlinear susceptibility is a tensor, which depends on the symmetry of the nonlinear optical material. For example, $\chi^{(2)}$ is a third-rank tensor with 27 Cartesian components. A complete description of the nonlinear interaction in the case of SFG, therefore, requires 12 of these tensors yielding a total of 324 different and possible complex components that need to be specified.[88,89] Fortunately, intrinsic permutation symmetry and crystal symmetry decrease the number of independent components. This makes nonlinear optical effects (e.g., SHG DFG, THG, FWM, Figure 3.1) a very sensitive method for probing the crystal symmetry of given materials.[88,89] Furthermore, the second-order or other even-order nonlinear optical effects can only occur in a material that lacks the centre of inversion symmetry. Therefore, the second-order nonlinear optical effects, such as SHG, are dipole-forbidden in centrosymmetric materials. However, second-order nonlinear optical effects can occur at the surface (or interface) of a centrosymmetric material by surface (or interface) induced symmetry breaking [90]. On the contrary, third-order nonlinear optical

effects are allowed in all materials regardless of the crystal symmetry. Nevertheless, the components both second-, third-, and high-order susceptibility tensors all strictly depend on the crystal symmetry of the materials. Nevertheless, SHG, THG and HHG can be very sensitive to the orientation of the sample and the polarization of the incident field. For these reasons, nonlinear optical processes provide a convenient method for probing the crystal symmetries of various materials.

Research on nonlinear optics is growing daily and the field of nonlinear optics plays a major role in emerging photonic and optoelectronic technologies, such as coherent laser sources, signal processing, ultrafast switching, ultrashort pulsed laser, imaging, sensors and so on (Figure 3.2). Thus, it has attracted huge interest, and this has led to significant progress over the past decade. In below Sections, the current state-of-the-art 2D materials based representative NLO processes is presented.

3.2 Harmonic generations in 2D materials

After the first experimental demonstrations of harmonic generation in 2D materials (e.g., surface SHG in graphene [91], SHG in MoS_2 [22,92-95], THG from graphene [45,46] and MoS_2 [96-99]), significant research efforts have been directed to this topic. Since then, demonstrations of SHG and THG have been reported from a wide range of monolayer and few-layer 2D materials, including BP [100-102], WSe_2 [21,25,103,104], WS_2 [105-108], $MoSe_2$ [109,110], GaSe [111-115], GaTe [116], h-BN [92,117,118], $MoTe_2$ [119-121], InSe [122], ReS_2 [123], CrI_3 [124], and $AgInP_2S_6$ [125]. Most of these results have revealed that 2D materials exhibit exceptionally large NLO susceptibilities (e.g., $\chi^{(2)} \approx 10^{-7}$ mV^{-1}) [92,93], implying huge potential of these materials for various applications (e.g., ultrafast pulse characterization [126], telecom wavelength conversion [127,128]).

3.2.1 Second-harmonic generation

The lack of inversion symmetry in a material can give rise to a strong SHG signal under an intense optical pump. The observation of SHG in monolayer MoS_2 with ~800 nm excitation wavelength was reported in References [20,22,129]. It demonstrated that SHG in monolayer MoS_2 is orders of magnitude larger than that of bilayer or bulk MoS_2, as expected from their crystal symmetry properties.[129] Note that SHG signal also has been observed in monolayer graphene[91,130], even-number layered MoS_2 [131] and WSe_2 [132] flakes, and spiral WS_2 nanosheets [133] by symmetry breaking. In addition to the NLO response at the wavelength of ~800 nm, another interesting wavelength range is ~1550 nm, commonly used for optical telecommunication related applications. With the fundamental wavelength close to 1550 nm, the reported $\chi^{(2)}$ values (i.e., in the range of few pmV^{-1} for MoS_2 [97,134,135] and $MoSe_2$ [109,110]) are clearly lower than that measured with 800 nm lasers. The difference between measured results at 800 nm and 1550 nm was attributed by the exciton resonant enhancement.[109]

The effects of strongly bound excitons on the SHG in monolayer TMDs have attracted much attention.[20,21,109,136] Reference [20] tuned the excitation wavelength from ~680 to 1080 nm to study the wavelength dependence of the SHG in monolayer MoS_2. It was found that the SHG intensity is significantly enhanced when the SHG wavelength overlaps with the energy of the C exciton (~2.8 eV), as shown in Figure 3.3(a). Second-order sheet susceptibility value of ~8×10^4 pm^2 V^{-1} was reported, when the SHG is in resonance with the C exciton.[20] The C exciton was further indicated as the band nesting region with singularities of the joint density of states.[94] For comparison purposes, an effective bulk-like second-order NLO susceptibility is typically obtained by dividing the sheet susceptibility with the thickness of the monolayer (e.g., 0.65 nm for MoS_2) yielding an effective bulk-like second-order susceptibility of ~0.1 nm V^{-1}.[20] Roughly similar values were also reported for MoS_2 in other studies [129,137] as well as for WS_2 [105] and WSe_2 [103] at the same wavelength range. The SHG has also been found in the symmetry materials by exciting the electric-quadrupole term of second-order susceptibility. For example, graphene has been found with strong SHG by optical dressing an in-plane photon wave vector and proper carrier doping.[58] In addition, by stacking graphene into twisted bilayer graphene, the inversion symmetry is broken at typical angel and a strong SHG has been observed, which introduces a new way of symmetry engineering for SHG process.

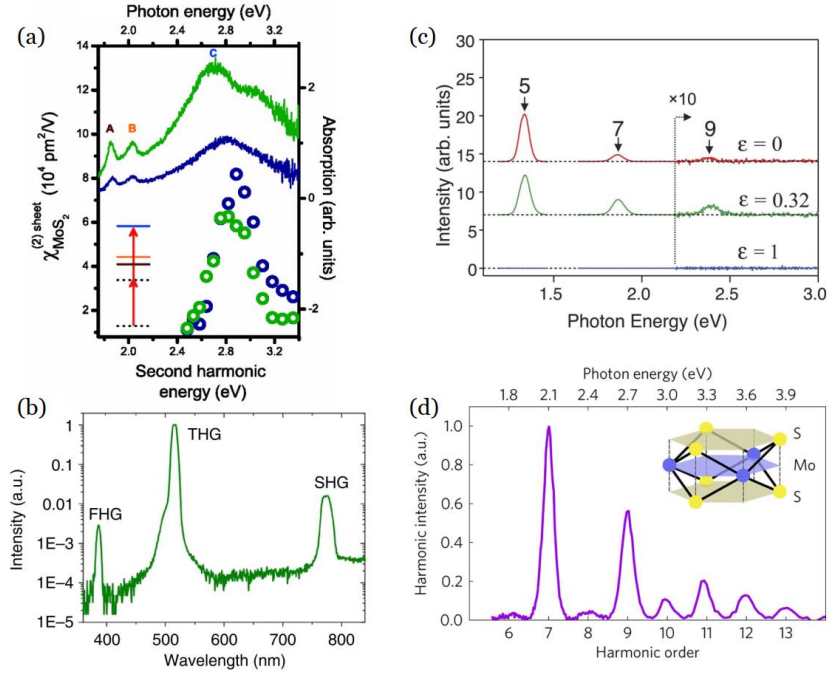

Figure 3.3. Harmonic generation in 2D materials: (a) Measured absorption (solid lines) and second-order susceptibility (circles) of MoS_2. Data shown on blue is from monolayer and green is from tri-layer MoS_2. Exciton peaks (i.e., A, B and C) are also indicated.[20] (b) SHG, THG and FHG in monolayer MoS_2. Inset: THG image of a MoS_2 flake.[134] (c) HHG in monolayer graphene with different polarized light excitations.[51] (d) HHG in monolayer MoS_2.[138]

In monolayer TMDs, the two polarization components of SHG depend on the crystal orientation as [129]: $I_{||}=I_0\cos^2(3\theta)$ and $I_{\perp}=I_0\sin^2(3\theta)$, where θ is the angle between the mirror plane and the input light polarization, I_0 is the maximum intensity of the SHG [129], and $I_{||}$ and $I_{\perp}$ are the SHG intensity components parallel and perpendicular to the input light polarization, respectively. Therefore, SHG can be efficiently utilized to probe the crystallographic orientation of 2D materials, by measuring the SHG intensity parallel or perpendicular with the excitation polarization direction.

3.2.2 Third-harmonic generation

In contrast to SHG, THG can be possibly observed in materials regardless of symmetry selection rules. References [44-46] reported on the observation of THG in graphene. For instance, Reference [46] obtained a $\chi^{(3)}$ value of graphene by comparing the THG signal from graphene to that of SiO_2 based substrates (e.g., fused silica), reporting that $\chi^{(3)}$ of graphene (~10^{-19} m^2 V^{-2}) is nearly 3 orders of magnitude larger than that of fused silica (~ 2.5×10^{-22} m^2 V^{-2}).[88,89] Note that the reported $\chi^{(3)}$ values of graphene measured with various excitation wavelengths range from ~10^{-15} m^2 V^{-2} [19,44] to ~10^{-19} m^2 V^{-2} [97,139]. Such a large deviation between the measured values reflects the challenge in accurate measurement of optical nonlinearity of nanomaterials. On the other hand, the large deviation of the measured $\chi^{(3)}$ values in graphene also highlights that the optical nonlinearity in graphene and other 2D materials can be very sensitive to various parameters (e.g., substrates [140-142], defects [143], doping [141], strain [144], chemical treatment [98]). Despite these deviancies, it is clear that 2D materials possess large third-order susceptibilities potentially for a wide range of applications. Other 2D materials (e.g., MoS_2 [97,98,134] in Figure 3.3(b), BP [100-102], and GaSe [111]) have also been shown to possess $\chi^{(3)}$ in the same range as graphene for relatively large THG. In addition, it has been demonstrated that THG can be used as a rapid and large-area characterization method for determining the crystallographic orientations of exfoliated BP [100] and the grain boundaries of chemical vapor deposited TMDs[98].

3.2.3 High-harmonic generation

High-harmonic generation (HHG) can provide an alternative light source in the deep ultraviolet or even the X-ray spectral range, which has been widely used to produce pulses with attosecond [145] (or even zeptosecond [146]) durations for various fundamental research experiments (e.g., monitoring electronic motion inside materials). Traditionally, HHG is observed from atomic gases [147,148] and more recently from various bulk crystals (e.g., ZnO [149], and GaSe [150]). However, the underlying mechanism of HHG in bulk solids is still under debate.[138]

HHGs that were experimentally observed in graphene [51] and MoS_2[138] might provide some indications for the behind mechanism. Reference [51] studied the 5^{th} , 7^{th}, and 9^{th} harmonics in graphene, and observed that HHG signal in graphene is dramatically enhanced under elliptically polarized excitation

(Figure 3.3(c)), in which the ratio between the bandgap and Rabi frequency in graphene strongly affects the HHG performance.[51]

MoS_2 with a finite bandgap is different from zero-gap graphene.[51] Reference [138] studied the HHG in MoS_2 with an intense mid-IR excitation (0.3 eV), as shown in Figure 3.3(d). It reveals that generated harmonics up to the 13^{th} order emerge in the visible range, where the odd-order harmonic efficiency per layer exhibits significant enhancement compared to the bulk, which is attributed by the electronic correlation effects.[138] Furthermore, the band nesting effect has been found to contribute the strong even-order HHG, which further indicates contribution of the interband transitions.[151] These key findings of these proof-of-principle HHG results observed in monolayer [51,138,152,153] and thick-layer [154] materials suggest that much more research efforts are likely to come in the near future, which would fully discover the potential mechanisms behind the HHG.

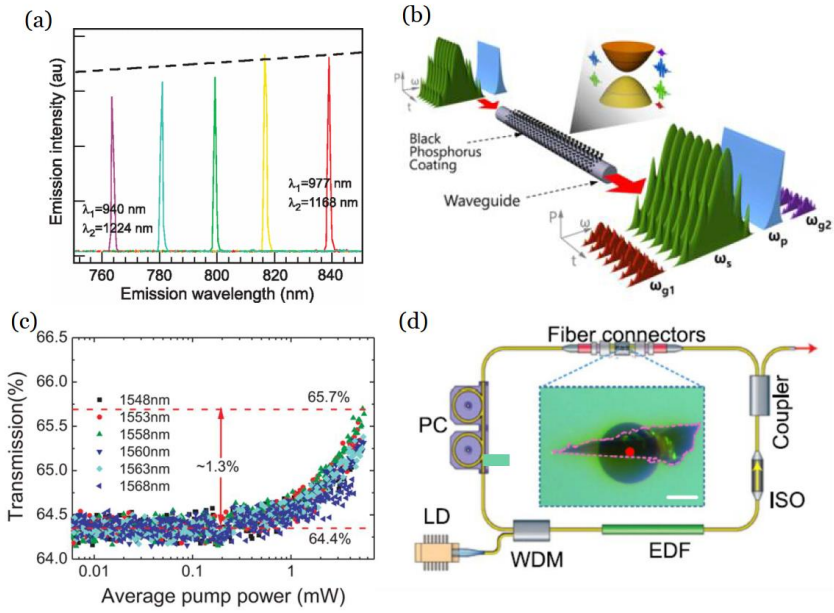

Figure 3.4. (a) FWM spectra of a graphene flake excited with pump pulses at different wavelengths. The dashed line represents the wavelength dependence predicted by nonlinear quantum response theory.[19] (b) Schematic illustration of FWM-based wavelength conversion in a BP-deposited integrated fiber device. Inset: bandgap of BP.[155] (c) NLO absorption of graphene at different wavelengths.[31] (d) A typical configuration of 2D materials based ultrafast fibre lasers. Inset: an optical image of a BP (marked by pink dotted line) integrated fiber device. The red dot indicates the optical fibre core. PC: polarization controller; LD: laser diode; WDM: wavelength division multiplexer; EDF: Erbium-doped fiber; ISO: isolator.[156]

3.3 Four-wave mixing

Four-wave mixing (FWM) is widely employed for various applications, such as wavelength conversion, optical signal amplification, imaging, and many other

light manipulation applications.[88,89] Graphene-based FWM was first reported in the near-infrared region.[19] Figure 3.4(a) shows the measured NLO response of monolayer graphene as a function of the emission wavelength for several combinations of pump wavelength λ_1 and λ_2, where the large FWM signal is usually attributed to the coherence of NLO processes with the strong interband electron transitions.[19] By integrating 2D materials with various photonic structures (e.g., photonic crystal cavities [47], micro-ring resonators [157], microfibers [158,159]), FWM based NLO devices have been realized. For example, high *Q*-factor silicon photonic crystal microcavity has been used to demonstrate cavity-enhanced FWM in graphene.[47] The conversion efficiencies were observed up to 10^{-3} at a cavity *Q*-value of 7500 with a low pump power of 600 μW.[47] Another example is to integrate BP into microfiber to achieve ultrafast optical switching with FWM, as shown in Figure 3.4(b).[155] FWM induced wavelength conversion was enhanced by depositing BP on a D-shaped optical fiber, with an estimated conversion efficiency of ~10^{-7}, indicating that BP could provide a good platform for ultrafast optical switching at high speed up to 20 GHz.[155]

3.4 Saturable absorption

Saturable absorption effect in 2D materials has been widely used in ultrafast fiber lasers.[160,161] These lasers with output pulse duration in picosecond or femtosecond timescale can be constructed by placing a saturable absorber inside a laser cavity. While the real part of the third-order NLO susceptibility (i.e., Re($\chi^{(3)}$)) is responsible for typical third-order NLO processes (e.g., FWM and THG), the imaginary part (i.e., Im($\chi^{(3)}$)) dominates the nonlinear absorption such as multi-photon absorption, optical limiting, and SA property.[162] Note that higher-order susceptibility (e.g., Im($\chi^{(5)}$)) can also contribute to SA.

In the past decade, the demonstration of graphene based saturable absorbers has created a new paradigm for building ultrafast pulsed lasers.[69,163-166] Figure 3.4(c) shows a graphene SA at different pump wavelengths, which indicates its broadband operation property. A typical 2D material integrated fiber laser is shown in Figure 3.4(d). More recently, other 2D materials have also been demonstrated for saturable absorbers (e.g., MoS_2 [167-172], WS_2 [172-175],WSe_2 [176], ReS_2 [177], BP [178-182] in Figure 3.4(d)). Thus far, 2D materials have been integrated in various lasers (such as solid-state [129,183-186], waveguide [187], fiber [69,165,166,179,188-193], and semiconductor [194] lasers) to generate ultrashort optical pulses.

3.5 Difference-frequency generation

Difference-frequency generation (DFG) is of great significance a large range of applications. It plays the main role for generating coherent light at longer wavelengths and acts as the base for other second-order nonlinear parametric interactions such as optical parametric generation (OPG), amplification (OPA) and oscillation (OPO), which enable to produce tunable light sources across

different spectral regions for a large variety of applications including material characterizations, laser spectroscopy, and molecular sensing.[195]

Along with SHG, SFG, the exploration of DFG, a frequency down-conversion process in 2DMs would extend the application range of nonlinear optics. Thus far, DFG in graphene has been observed in terahertz region.[196] With symmetry broken, the DFG in TMDs has been observed within single layer thickness. Figure 3.5(a) plots the spectra of DFG process: an idler output under the excitation of pump and signal pulses. The idler power shows the linear relationship with the pump and signal power (Figure 3.5(b, c)). The generated idler power indicates an effective second-order nonlinear susceptibility ~1.8×10^{-8} m/V, comparable to other reported values.[20] The maximum quantum conversion efficiency from the pump to the idler in this DFG process is calculated as ~2×10^{-4}.

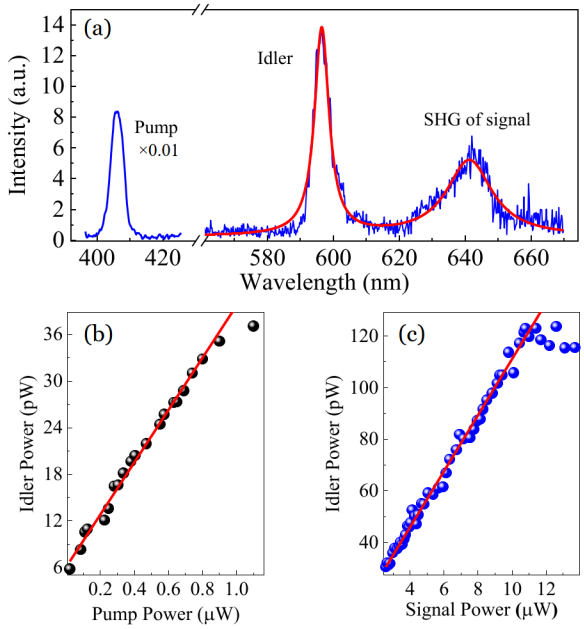

Figure 3.1. DFG process in monolayer MoS_2. (a) The generated DFG spectrum; (b) DFG power of the idler at 595 nm as a function of the pump power with the signal power fixed at ~2.5 μW; (c) The DFG idler power dependence on the signal power with the fixed pump power at ~0.9 μW. Adapted from Publication 1.

The single-layer thick TMDs physically limits the light–matter interaction length. By employing the thicker sample such as 3R-type bulk MoS_2 with broken inversion symmetry, the higher DFG conversion efficiency would be realized.[197] On the other hand, with external cavities (such as photonic-crystal nanocavity, micro-ring resonator, whispering-gallery cavity and metallic plasmon), or waveguides (including microfibers, on-chip waveguides) is also promising for further improvements. With these methods, the possible observable OPA is expectable. Further, with proper assistance of the cavities, OPO operation with 2D materials could be achieved.[198]

3.6 Engineering nonlinear optical responses

Active and efficient control of optical responses is the major function for optical signal processing, which is intrinsically connected to the nonlinear optics. In 1962, electrically tunable SHG have been achieved at the surface of calcite crystal by inducing a third-order optical nonlinearity with a DC electric field.[199] In 2D materials, tunable nonlinear optical responses have been largely developed, mainly depending on the tunable resonant optical transitions. Figure 3.6(a) shows a structure with monolayer MoS_2 to electrical tune optical nonlinearity. With the device, FWM signals at A, B excitons have been electrically tuned with around 80% depth, while that without exciton assistance remains unchanged (Figure 3.6(b)). The electrically tunable SHG with similar structure has also been demonstrated in WSe_2.[136] On the other hand, the tunable THG and FWM have been reported in graphene with help of Fermi level and hot carriers [63,64], of which the linear dispersion of Dirac fermions promises a wideband optical tunability. The gate dependent nonlinear optical responses can be further developed into waveguide integrated devices [65,200] and ultrafast fiber lasers [66]. Tunable nonlinearities in 2D materials offer many advantages, such as fast speed and compact footprint, for the future optoelectronic applications.

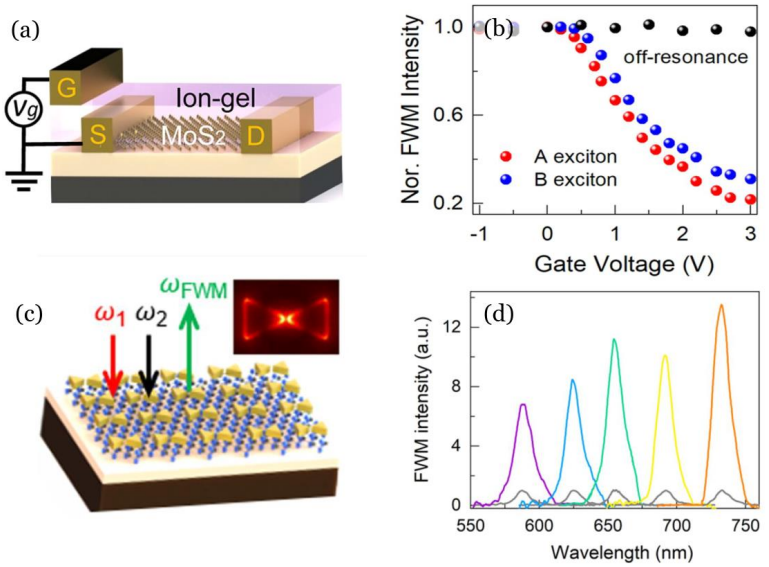

Figure 3.2. (a) An illustration of a MoS_2 tunable nonlinear optical device. (b) Gate tunable FWM at A (~650 nm), B (~610 nm) excitonic states and off-resonance (~700 nm). (c) An illustration of enhanced FWM from a hybrid MoS_2-plasmonic structures. Inset: simulated electric field enhancement in the plasmonic structure. (d) Experimental FWM signals at different wavelengths from the hybrid MoS_2-plasmonic structure (coloured curves) and bare MoS_2 (gray curves). Figures (a) and (b) are adapted from Publication 8. Figures (c) and (d) are adapted from Publication 9.

However, the atomic thickness of 2D material limits the length of its nonlinear interaction with light. The absolute conversion efficiency is still low, typically around 10^{-10}. Further development to enhance the nonlinear optical interaction

is necessary. In fact, various platforms, such as optical cavity [47,201], plasmons [202], metasurface [203] have been explored to enhance the optical nonlinearities.[204] Figure 3.6(c) gives an example of bowtie based plasmons enhanced FWM. The enhancement of FWM signals with such structure can be achieved with one order of magnitude, as shown in Figure 3.6(d). The equivalent third-order nonlinearity of the hybrid MoS_2-plasmonic structure is in the order of 10^{-17} m^2/V^2, superior (~10–100-time larger) to the widely used conventional bulk materials (e.g., $LiNbO_3$, BBO) and nanomaterials (e.g., gold nanofilms).

Although the nonlinearities including second- and third-order susceptibility in 2D materials have been significantly increased via various advanced methods (e.g. cavities, plasmonic, and waveguides), the current development of 2D materials for the practical applications remains elusive. Nevertheless, further investigations on physics and characterizations in 2D materials could deepen the understanding of the nonlinear optical phenomena and potentially pave a way for advanced applications in the field of optoelectronics and nanophononics.

4. Transient linear and nonlinear absorption in monolayer MoS_2

The topic of light–matter interaction in semiconductors has raised a remarkable interest for various photonic and optoelectronic applications, which is intrinsically determined by the bandgap of the materials involved. To extend the applications beyond the bandgap limit, it is important to study the light–matter interaction below the material bandgap. In this chapter, we study ultrafast optical absorption of monolayer MoS_2 in its sub-bandgap region from ~0.86 μm to 1.4 μm under the ultrafast pump light excitation. Our objective would elucidate the fundamental understanding regarding the optical properties, excited carrier states, and carrier dynamics in the technologically important near-infrared region, which potentially lead to various photonic and optoelectronic applications (e.g., excited-state-based photodetectors and modulators) of two-dimensional materials and their heterostructures beyond their intrinsic bandgap limitations.

4.1 Linear optical properties in monolayer MoS_2

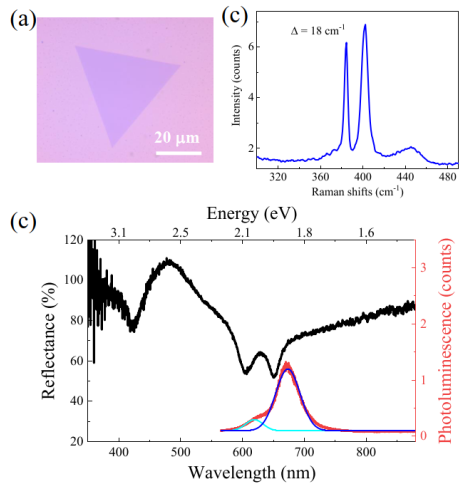

Figure 4.1. Optical characterization of monolayer MoS_2. (a) Microscope image, (b) Raman spectrum, where Δ is the difference between two Raman peaks. (c) Linear reflection (black) and photoluminescence (red) spectra. The blue and violet curves are the Lorentz fitting corresponding to the A, B excitonic resonances. Adapted from Publication 1.

We use monolayer MoS_2 as a typical representative of TMDs. Monolayer MoS_2 is grown on a SiO_2/Si substrate (the thickness of SiO_2: 285 nm) via vapor-liquid-solid method. First, ~2 mg/mL Na_2MoO_4 aqueous solution was spin-coated on the substrate at 6000 rpm for 30 seconds. Then, the Na_2MoO_4 coating is sulfurized in sulphur vapor to obtain monolayer MoS_2 at 750 °C for 5 min.[205,206] As shown in Figure 4.1(a), the MoS_2 flake has a triangle shape. The Raman measurement (Figure 4.1(b)) is performed with peaks of an in-plane mode (E_{2g}) located at ~384 cm^{-1}, and an out-of-plane mode (A_{1g}) at ~402 cm^{-1}. The difference between these two modes is around ~18 cm^{-1}, indicating the monolayer structure.[207] Further, the monolayer MoS_2 flake is characterized by linear optical reflection and photoluminescence measurement. As shown in Figure 4.1(c), the three dips at ~421 nm, 604 nm, 650 nm, appear in the reflection spectrum (black curve), corresponding to the C, B, A excitons. In the meantime, the photoluminescence spectrum (red curve) is also plotted in Figure 4.1(c). Two photoluminescence peaks (~619 nm and ~673 nm, corresponding to B, A excitons) are obtained by Lorentz fitting, shown as the violet and blue curves. The peak positions are slightly red-shifted comparing with the dips of the reflection spectrum, due to large binding energy in the confined structure. Thus, the experiments indicate that our CVD-grown MoS_2 flakes are typically monolayer with relatively high quality.

4.2 Pump-probe optical setup

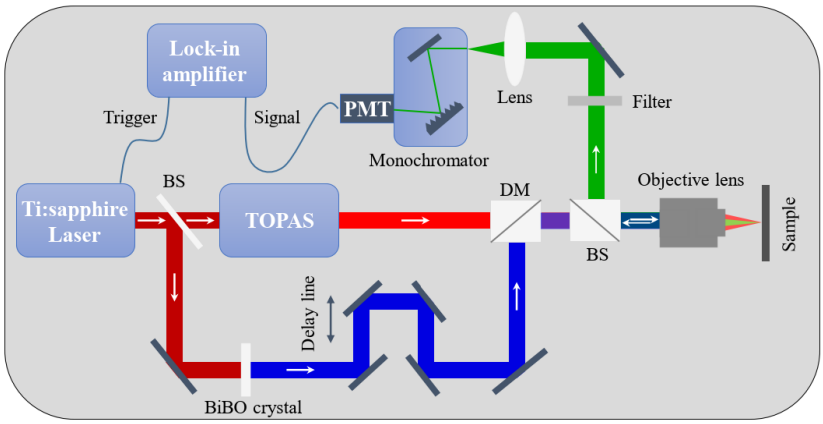

Figure 4.2. Pump-probe setup. BS: beamsplitter, DM: dichroic mirror, PMT: photomultiplier tube. Adapted from Publication 1.

To perform the transient optical interaction, we built an experimental setup as shown in Figure 4.2. Femtosecond (~220 fs) pulses from an amplified Ti:sapphire laser system at the wavelength of ~812 nm with a repetition rate of 2 kHz are employed as a light source. The output beam is first divided into two beams, one is applied for the generation of pump pulses at ~400 nm via frequency doubling with a BiBO crystal and the other for generating the tunable near-infrared pulses (~1300 to 1550 nm) by pumping a TOPAS system (Light conversion). The

pump and idler beams are combined by a dichroic mirror (DM) and then focused by an objective (40×, NA. 0.75) on the target sample. The full width at half maximum of the pump and idler beam spots is ~2.5 μm. A delay line is employed to synchronize pump and probe pulses. The probe is then collected with the same objective lens by a reflection configuration and finally focused into a monochromator followed by a photomultiplier tube (PMT). Colour filters are used in order to remove the residual pump light before the monochromator. A microscopy is installed in the system (not displayed here) with a white light illumination and a CCD camera to check the sample. This system is also used for the experiments carried in chapters 5 and 6 after minor modification.

4.3 Transient optical absorption

Ultrafast transient absorption (TA) properties of ML-MoS_2 flakes are explored in the NIR region from ~0.86 to 1.4 μm wavelength and investigated with its ultrafast carrier dynamics when excited by the pump light at 400 nm in a reflection geometry. The normalized time-resolved absorption modulation (ΔA) mapping is shown in Figure 4.3(a), with an average probe power $P_s \simeq 1.5$ μW and average pump power $P_p \simeq 0.3$ μW. The zero-delay position is indicated by a black solid line, which is determined by the difference-frequency generation between the pump and probe pulses. Due to the presence of the pump, it clearly shows that the absorption of the probe beam in monolayer MoS_2 changes across the whole probe spectrum range. As shown in Figure 4.3(b), the time-resolved absorption modulation ($\Delta A = A_1 - A_0$) at the probe wavelength of ~1.13 μm is displayed, where A_1 and A_0 are the absorptions with and without the presence of pump light. The delay time $\Delta\tau$ is the relative time difference between the pump and probe pulses on the sample.

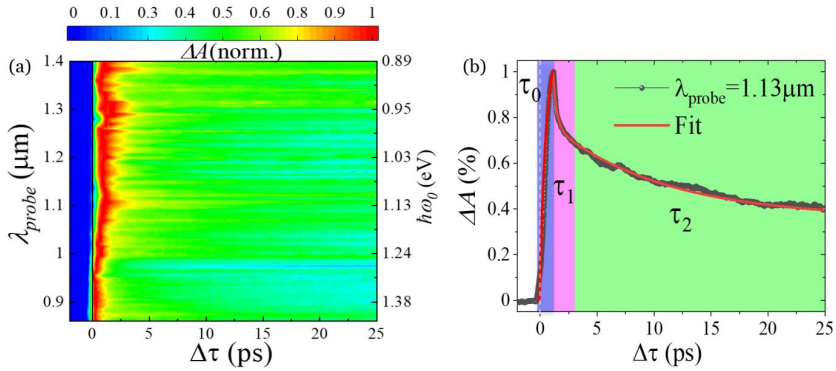

Figure 4.3. Broad transient absorption in the NIR region. (a) Mapping of normalized absorption modulation (ΔA) over the probe spectrum range from ~0.86 to 1.4 μm. Average pump power P_p (intensity I_p) is ~0.3 μW (~4.53 GW/cm^2) and average probe power P_s (intensity I_s) is ~1.5 μW (~28.93 GW/cm^2). (b) The time-resolved absorption modulation when the probe is at 1.13 μm. An illustration of rise time (τ_0), fast recovery (τ_1), and slow recovery (τ_2) time constants are labelled. The rising and decay curve fit with the single and bi-exponential function, respectively. Adapted from Publication 7.

The results clearly show TA modulation, which first rises and then decays. the rising of ΔA (marked in purple color) from zero to its maximum value is very fast. With the presence of pump light ΔA is immediately increased with a single-exponential rising time constant (τ_0 = ~538 fs). Once absorption modulation ΔA reaches its highest level, it starts to recover. At the beginning of the decay, the intensity of ΔA drops down to a certain level very quickly (marked in magenta color) and then decays slowly (marked in green color). Therefore, the decay dynamics can be fitted (red curve) by two exponential time constants (i.e., fast (τ_1) and slow recovery (τ_2) constants). At the probe wavelength 1.13 μm, the fitted τ_1 and τ_2 are ~1.02 ps and ~80.5 ps respectively. It is evident that the carrier dynamics is pretty independent of both pump and probe powers. Since the carrier dynamics did not exhibit a strong dependency on pump and probe fluence, therefore we can rule out exciton-exciton annihilation processes.

We therefore conclude that the enhancement of absorption in this wavelength range of our experiments (>~1μm) is due to the formation of the exciton, where the rising time constant τ_0 of ~477±80 fs is close to the time constant for exciton formation in ML-MoS_2 as reported in [208,209]. After ultrafast thermalization and formation and excited states, the hot carriers relax via a two-step process, which indicates the decay dynamics. The initial fast recovery is happening within the time range of ~1.05±0.39 ps, which is very well matched with the process of fast carrier capture due to defects as reported by Wang *et.al.* [210]. The invariant TA dynamics over pump power and linear increment of absorption modulation ΔA (Figure 4a) further ensure this process. The slow recovery component has a time constant of tens of picoseconds (~93.9±14 ps) corresponds to the carrier-phonon scattering.[41,211-213]

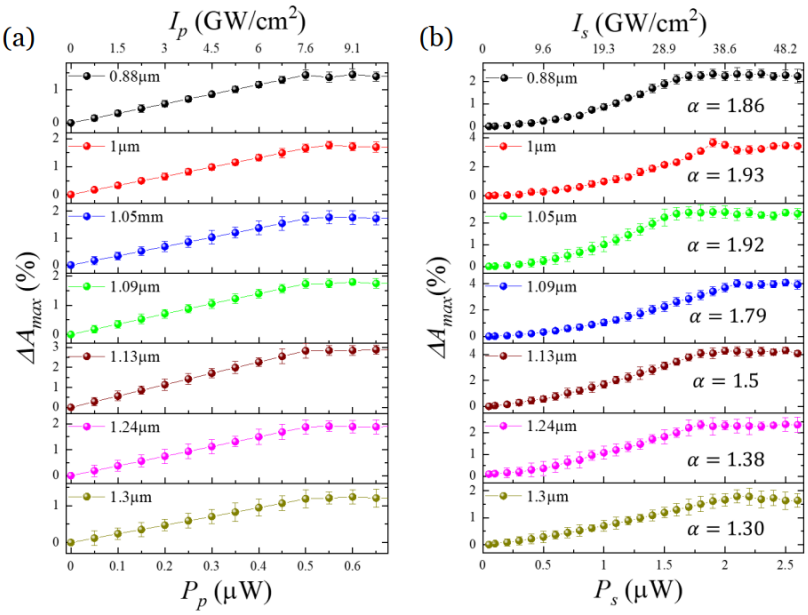

Figure 4.4. Power dependent of transient absorption (ΔA_{max}). ΔA_{max} at few selective probe light wavelengths w.r.t (a) pump and (b) probe light power with a fixed probe light power of 1μW and pump light power of 0.3μW respectively. Adapted from Publication 7.

Further, we studied both $P_p\,(I_p)$ and $P_s\,(I_s)$ dependent ΔA_{max} by keeping $P_s\,(I_s)$ and $P_p\,(I_p)$ constant successively with an appropriate delay time $\Delta\tau$ where ΔA is maximum. The dependency of ΔA_{max} on $P_p\,(I_p)$ by keeping $P_s\,(I_s)$ fixed at ~1 μW (~19.29 GW/cm²) is shown in Figure 4.4(a) for a few selective probe wavelengths. There is a linear relationship between ΔA_{max} and P_p at the beginning. When $P_p\,(I_p)$, reached ~0.5 μW (~7.55 GW/cm²) and beyond, ΔA become saturated and has no observable change within the error limit. The linear dependence of ΔA on P_p (i.e., $\Delta A_{max} \propto P_p$), indicates one-photon excitation and contribution process (i.e., one absorbed pump photon creates one excited carrier, and presents excited-state introduced absorption at the probe wavelength). Additionally, the saturation of absorption modulation ΔA_{max} for the pump beam power can be attributed to the deficiency of photo-excited carriers after the power crosses a certain threshold. The saturation can be caused by Pauli blocking, which explains the recently reported saturable absorption in TMDs and their applications in ultrafast pulse generation.[167]

Similarly, the influence of $P_s\,(I_s)$ on ΔA_{max} has been studied with a fixed $P_p\,(I_p)$ of 0.3 μW (4.53 GW/cm²) at different probe wavelengths as depicted in Figure 4.4(b). The observed maximum value of ΔA_{max} is as high as ~4.2% of the 1.13 μm probe wavelength. Here we observe nonlinear relation between P_s and ΔA_{max} at the beginning till to the saturation effect at high $P_s\,(I_s)$. The power dependence before saturation can be fitted with at $\Delta A_{max} \propto P_s^{\alpha}$ at fixed P_p, where α is the power-law coefficient. The value of α at different probe wavelengths is shown in the inset of Figure 4.4(b). Dependency of ΔA on P_s (i.e., $\Delta A_{max} \propto P_s^{\alpha}$) is nonlinear which signifies that two-photon absorption (TPA) phenomena at the probe wavelength takes place before it hits the saturation region. The value of α has a tendency to decrease with the increase of probe wavelength which indicates that the two-photon absorption is more dominant at the shorter probe wavelengths and becoming linear at the longer wavelength range. This is possibly due to the enhanced intraband absorption at a longer wavelength of the excited carriers, which is expected to be linear. Here, the saturation of absorption modulation ΔA_{max} for the probe beam power also can be attributed the Pauli blocking effect.

5. Transient second-harmonic generation in monolayer TMDs

Dynamic control of light-matter interaction is of significant importance for the generation, modulation, and detection of optical signals. Besides the linear absorption control in chapter 4, it is extremely fascinating to all-optically modulate nonlinear optical responses of materials for a large range of applications, such as optical data processing, optical communications[9], optical frequency comb generation, and quantum optics[214]. The efficient strategies to all-optically control the SHG process have still remained elusive, while it has been reported previously with metals[11] and semiconductors [12,13,15,215]. Novel all-optical modulation methods with new materials are thus of great significance for various emerging and future applications (e.g., on-chip nonlinear photonics).

In this chapter, we report a giant, ultrafast, and broadband modulation of second harmonic generation with excitons in monolayer MoS_2. Optically excited dark exciton states can significantly modulate SHG in MoS_2 with weak control light. Thanks to the strong excitonic effect, a giant enhancement factor of up to ~400 times is achieved at room temperature, one order of magnitude larger than the current state-of-the-art methods using metallic or semiconducting nanostructures. Moreover, the modulation amplitude and sign of SHG variation can be adjusted with various intra-excitonic dynamics, such as transitions associated with dark (e.g., 2*p*, 3*p*) and bright (e.g., 1*s*, 2*s*) states. Our results not only present a complementary method to the currently widely used linear absorption-based pump-probe spectroscopy for providing insights into the intriguing exciton dynamics of 2D materials, but also offer a new scheme for all-optical nonlinear photonic and optoelectronic based on excitons.

5.1 Second-harmonic generation

We first investigate SHG in monolayer MoS_2. The monolayer MoS_2 is grown on a SiO_2/Si substrate by using the chemical vapor deposition method with a ~10 mg sulphur (at 170 ^{o}C) and ~0.5/15 mg NaCl/MoO_3 mixture (at 750 ^{o}C) for 5 minutes in high purity Argon (same method in chapter 4). Figure 5.1(a) shows the typical optical image of MoS_2. The SHG is observed with a centre wavelength at 530 nm and bandwidth of 8.4 nm (Lorentz fitting) when the MoS_2 is illuminated with the femtosecond pulsed laser at 1060 nm (Figure 5.1(b)). Figure

5.1(c) gives the SHG signal with the relation of excitation light power. The measured SHG signal scales quadratically (~1.95) with the fundamental pump intensity, confirming the second-order nonlinear optical process.

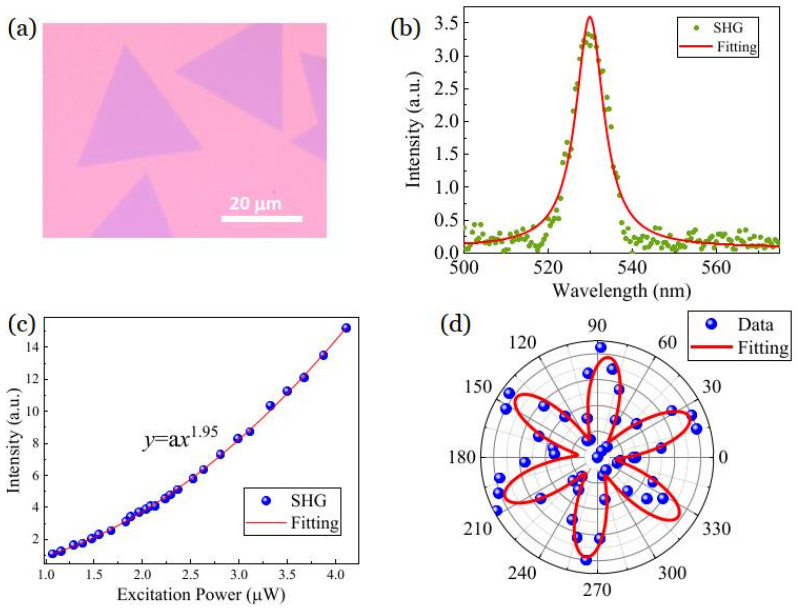

Figure 5.1. Second-harmonic generation in monolayer MoS_2. (a) Optical image of monolayer CVD MoS_2. (b) SHG spectrum at 530 nm. (c) Power dependence of SHG. (d) Polarization dependence of SHG. Adapted from Publication 3.

Since SHG is very sensitive to crystal symmetry, the polarization-resolved SHG offers crystallographic features of MoS_2. The monolayer MoS_2 has the D_{3h} point-group symmetry, the second-order susceptibility tensor has nonzero elements with $\chi^{(2)} = \chi^{(2)}_{yyy} = -\chi^{(2)}_{yyx} = -\chi^{(2)}_{xxy} = -\chi^{(2)}_{xyx}$, where x, y, z are crystalline coordinates. And x axis is along with the armchair direction, 30° with zigzag direction, where the mirror symmetry is broken. We have measured the polarization-dependent SHG by employing the linear polarized excitation pulses and the SHG is detected after a polarizer parallel to that of the incident polarization by rotating the sample step by step. Figure 5.1(d) shows the polarization dependent SHG. It displays a clear sixfold pattern, confirming D_{3h} symmetry with the relation of $P_x \sim \sin^2 3\theta$. Similarly, the relation of y element ($P_y \sim \cos^2 3\theta$) can be obtained when the polarizer is set perpendicular to the polarization of incident light.

The SHG process in monolayer TMDs with D_{3h} symmetry requires total angular momentum conservation during light–matter interactions, therefore exhibiting the valley-exciton locked selection rule.[216] For example, during the SHG process, the transition from the ground state to the exciton state at a K valley requires two σ+ fundamental photons and emits a σ- SH photon. While in the -K valley, the situation is opposite, i.e. with σ- incident photons and emitted σ+ SH photon. To observe this phenomenon, we use a σ- polarized incident light to excite the SHG. As shown in Figure 5.2, the SHG spectral components shows a

strong emission with σ+ polarization and almost zero of σ- polarization. The helicity contrast ($\frac{I^+-I^-}{I^++I^-}$) is calculated as ~96%, confirming the valley selection rule from the D_{3h} crystal symmetry.

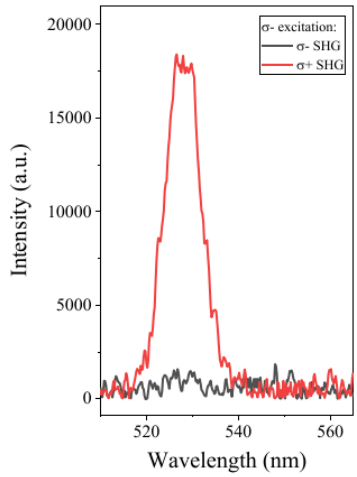

Figure 5.2. Generated spectra of σ+ SHG and σ- SHG when the incident fundamental light is 1060 nm with polarization of σ-. Adapted from Publication 3.

We further explore the wavelength-dependent SHG and uncover the C exciton enhanced SHG, similar to the previously published results.[20] By tuning the incident pulses with a wavelength range from 880 nm to 1160 nm and fixing the incident power at 2 μW, the broadband SHG is obtained as shown in Figure 5.3. Clearly, the strong enhancement of SHG is observed at 450 nm corresponding to the C exciton by comparing the linear reflection spectrum in Figure 4.1(c). And the largest enhancement is calculated with a ratio of 65 times with comparing maximum to minimum SHG. The C exciton is originated from the band nesting effect that occurs when conduction and valence bands are approximately equi-spaced over regions in the Brillouin zone. The band nesting region has singularities of the joint density of states and therefore results in a strongly enhanced optical response including linear and nonlinear effects.

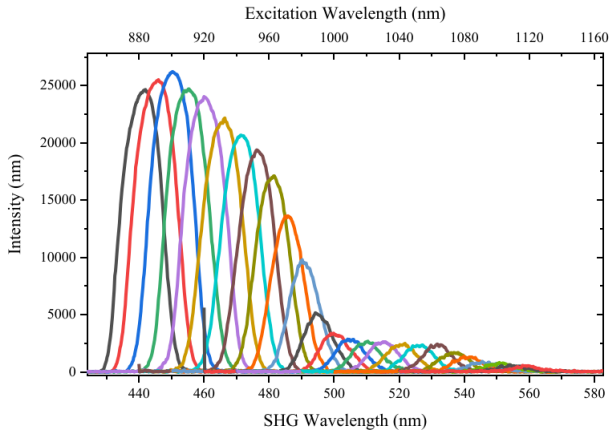

Figure 5.3. Wavelength dependent SHG in monolayer MoS_2. Adapted from Publication 3.

5.2 Transient second-harmonic generation in MoS_2

Figure 5.4(a) shows our simplified characterization setup, by which we study the SHG produced by seed light pulses as a function of delay time $\Delta\tau$ with respect to control light pulses in monolayer MoS_2 (Detail in Figure 4.2). We present a typical SHG modulation result in Figure 5.4(b), similar to the previously results.[217-224] A readily available control light of photon energy $\hbar\omega_c \approx 3.1$ eV ($\lambda_c \approx 400$ nm wavelength) above the C-exciton peak is chosen. The SHG signal at $\hbar\omega_{SHG} \approx 2.36$ eV ($\lambda_{SHG} \approx 525$ nm) generated by the seed light at $\hbar\omega_s \approx 1.18$ eV ($\lambda_s \approx 1050$ nm) is immediately enhanced by the control light with a single-exponential rising time constant ($\tau_0 \approx 600$ fs, orange fitted line). After $\Delta\tau \approx 1.3$ ps, the SH intensity starts to decay, exhibiting two exponential time constants ($\tau_1 \approx 4.4$ ps and $\tau_2 \approx 33$ ps, red fitted line). The SH spectra at $\Delta\tau$ = -1 and 1.3 ps are shown in Figure 5.4(c), which indicates strong SHG enhancement produced by the control light.

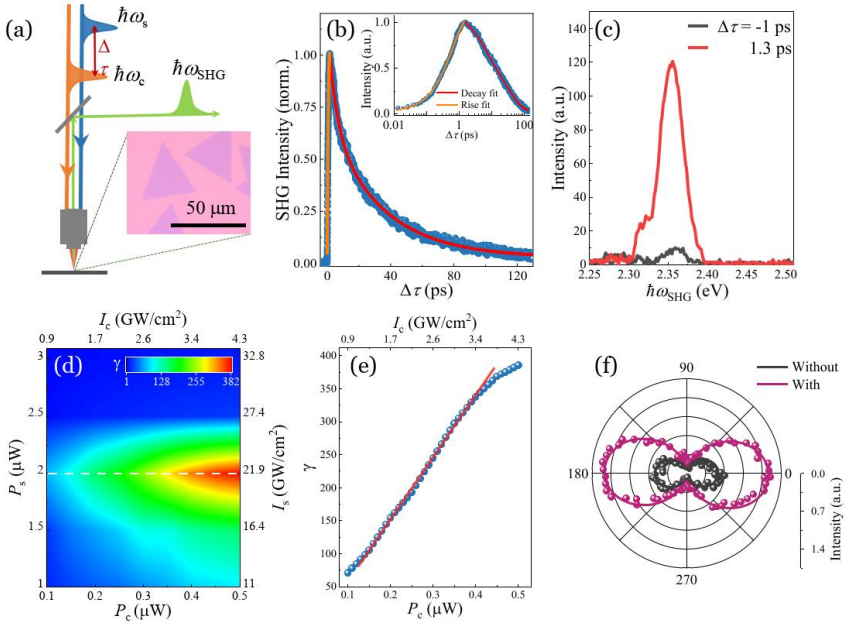

Figure 5.4. Giant SHG enhancement in MoS_2. (a), Sketch of the experimental setup. The inset shows an optical image of the MoS_2 flakes. (b), Normalized SHG intensity as a function of delay time $\Delta\tau$. The average power of the control and seed light is ~0.5 and ~2 μW, respectively. The pulse duration is ~230 fs. The inset shows a semi-log rendering of the same data. (c), SH spectra before and after the control light excitation. (d), SHG enhancement factor γ as a function of input power/peak-intensity of the control (P_c, I_c) and seed (P_s, I_s) light. (e), γ as a function of the control light power/intensity for P_s=2 μW (data along the white dashed line in d). (f), Polar plot of the circular-polarized SHG measured after passing a quarter-wave plate with and without the control light using σ- seed light. In (b)-(e), $\hbar\omega_c \approx$ 3.1 eV. In (d)-(f), $\Delta\tau$ = 1.3 ps. In (b)-(f), $\hbar\omega_{SHG} \approx$ 2.36 eV. Adapted from Publication 3.

Figure 5.4(d) shows the enhancement factor γ at $\Delta\tau$ = 1.3 ps as a function of the control and seed light powers. The value of γ is defined as $\gamma = P_w/P_{wo}$, where P_w and P_{wo} are SHG powers with and without the control light, respectively. We find that γ is highly dependent on incident light power. Figure 5.4(e) represents γ as a function of control light power when the average seed light power (peak intensity) is ~2 μW (~21.9 GW/cm^2). We find that γ increases linearly with the control light power (P_c) and is slightly saturated when P_c is > 0.4 μW (corresponding to a light intensity of ~3.43 GW/cm^2, equivalent to an electron-hole (*e*-*h*) pair density of ~5.7×10^{14} cm^{-2} considering the measured absorption of ~7.1% at ~3.1 eV). In Figure 5.4(e), γ reaches a maximum of 386 (with a corresponding enhancement of ~19 times in second-order nonlinear optical susceptibility). Similar enhancement phenomena are observed when the control light energy is changed to ~1.55 eV (λ_c = 800 nm) due to two-photon excitations.

Furthermore, we characterize the valley selection rule with and without control light. When switching on and off the control light, the polarization directions of SHG after passing a quarter-wave plate are almost the same (fitted parameters, Figure 5.4(f)), indicating that only σ+ polarized SHG is enhanced. This proves that symmetry remains conserved with control light excitation.

To explore the modulation mechanism, we measure the temporally and spectrally resolved SH fractional power changes ($\Delta P_{SHG} = (P_w\text{-}P_{wo})/P_{wo}$) at different seed energies ($\hbar\omega_s$ from 0.92 to 1.44 eV) with a fixed control light energy of 1.55 eV. Figure 5.5(a) shows an overview of the broadband wavelength-dependent SHG modulation dynamics. The SHG is enhanced (i.e., $\Delta P_{SHG} \geq 0$) by the control light when $\hbar\omega_{SHG}$ (λ_{SHG}) ranges from ~2.07 to 2.56 eV (~598 - 485 nm). We name this spectral range as the "enhancement region". A representative result when $\hbar\omega_{SHG} \approx$ 2.27 eV is plotted in Figure 5.5(b), showing a dynamic similar to that in Figure 5.4(b). When $\hbar\omega_{SHG}$ ranges from ~2.64 to 2.88 eV (i.e., ~470 - 430 nm) or from 1.84 to 2.07 eV (i.e., ~675 - 598 nm), the SHG is suppressed (i.e., $\Delta P_{SHG} \leq 0$) with the control light. We mark this spectral range as the "suppression region". A representative result is shown in Figure 5.5(c) when $\hbar\omega_{SHG} \approx$ 2.85 eV. In the suppression region, ΔP_{SHG} drops sharply in the presence of the control light and reaches its minimum within $\Delta\tau \approx$150 fs, faster than our measured temporal resolution (220 fs). Then, ΔP_{SHG} recovers with bi-exponential time constants $\tau_1 \approx$ 590 fs and $\tau_2 \approx$ 96 ps. Between the above-mentioned enhancement and suppression regions in Figure 5.5(a) (i.e., ~2.56 - 2.64 eV), the results typically show an extremely fast decay ($\Delta\tau \approx$150 fs) followed by fast recovery with a single-exponential time constant of ~600 fs. An example of this behaviour with $\hbar\omega_{SHG} \approx$ 2.58 eV is plotted in Figure 5.5(d). We denote this spectral region as the "transition region".

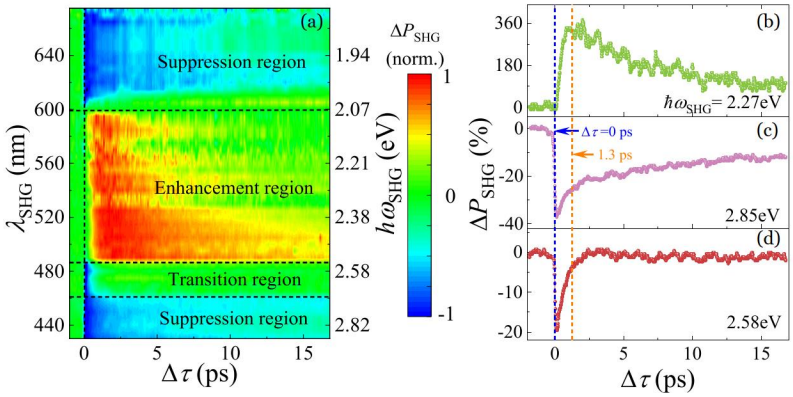

Figure 5.5. Broadband all-optical SHG modulation dynamics in MoS_2. (a), Normalized SHG change ΔP_{SHG} as a function of time delay and SHG photon wavelength/energy. The vertical black dashed line indicates $\Delta\tau$ = 0 ps position. (b)-(d), ΔP_{SHG} response for $\hbar\omega_{SHG}$ ~2.27, 2.85, and 2.58 eV, respectively. Blue and orange dashed lines mark $\Delta\tau$ = 0 and 1.3 ps. We use $I_c \approx 17.42$ GW/cm^2, $\hbar\omega_c \approx 1.55$ eV, and $I_s \approx 32.85$ GW/cm^2. Adapted from Publication 3.

In our measurements (Figure 5.5), the time-resolved dynamics are almost independent of the seed and control light powers, whereas the relative SHG change (ΔP_{SHG}) is linearly related with the control light power in all three regions using the 3.1-eV control light. Therefore, we can rule out an exciton-exciton interaction effect (e.g., exciton-exciton annihilation and Auger recombination), which commonly exhibit a nonlinear excitation power dependence. We thus can attribute the SHG modulation effects (i.e., enhancement and suppression) to various excitonic transition processes (e.g., scattering, transition, and recombination) in monolayer MoS_2.

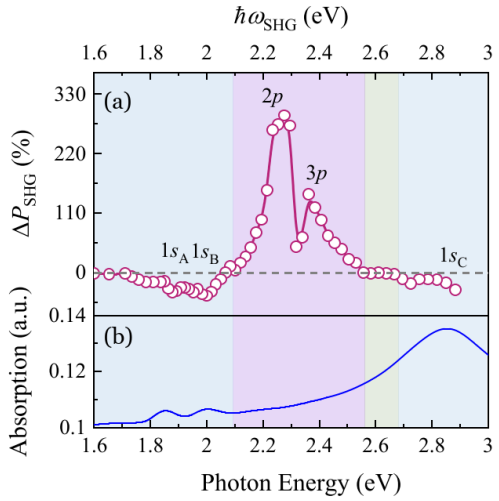

Figure 5.6. Maximum SHG modulation ΔP_{SHG} and optical absorption in monolayer MoS_2. (a) SHG change ΔP_{SHG} in monolayer MoS_2 when $\Delta\tau$ = 1.3 ps, $\hbar\omega_c \approx 1.55$ eV, I_c

≈ 17.42 GW/cm^2 and $I_s \approx$ 32.85 GW/cm^2. (b) Absorption spectrum of monolayer MoS_2. Adapted from Publication 3.

To gain further understanding, we plot ΔP_{SHG} as a function of the SHG photon energy (Figure 5.6(a)) for fixed seed and control light intensities with a delay $\Delta\tau \approx$1.3 ps, where the maximum enhancement is achieved. We find that the minimum dip positions in the suppression region are well correlated with the energies of 1*s* bright exciton states (e.g., $1s_A$, $1s_B$, and $1s_C$, where the subscript denotes the exciton species) in the linear absorption spectrum of monolayer MoS_2 (Figure 5.6(b)). We thus attribute the observed suppression of SHG to optical bleaching of bright excitons: the control light excites carriers from the ground state into quasi-continuum states with a single-photon excitation process at 3.1 eV (two-photon excitation at 1.55 eV), and the ground state becomes consequently depleted. The depletion suppresses the formation of bright excitons, blocks the typically observed bright excitonic resonance enhancement effect of SHG, and thus reduces the SHG signal.[20] The bleaching process is typically fast (normally <100 fs) [208,225], which fits well with the dynamics in the suppression region (Figure 5.6(b)). The subsequent bi-exponential recovery process in the suppression region can be correlated with different carrier relaxation processes, which gradually relax to the ground carrier states: an initial period of fast recovery with characteristic time $\tau_1 \approx$590 fs can be attributed to carrier cooling dynamics and formation of bright excitons; a slow recovery with a time constant $\tau_2 \approx$ 96 ps can be attributed to carrier-phonon scattering and nonradiative carrier recombination. This bi-exponential recovery process is similar to what has been previously reported in linear-absorption-based pump-probe measurements on bright excitons.

Additionally, there are two strong enhancement peaks at ~2.27 and 2.36 eV in Figure 5.6(a), which are far away from the A and B excitons. We verify that these two enhancement peaks are not featured in either the linear inter-band absorption spectrum (Figure 5.6(b)) and the wavelength dependent SHG spectrum (Figure 5.3). Furthermore, as shown in the time-resolved results of Figure 5.5(a), the initial rise time of SHG modulation in the enhancement region ($\tau_0 \approx$ 600 fs) is much longer than that in the suppression region (typically ~150 fs,). This indicates a completely different carrier dynamics, which excludes various simultaneous or ultrafast nonlinear effects, including ultrafast optical bleaching and optical parametric interactions.

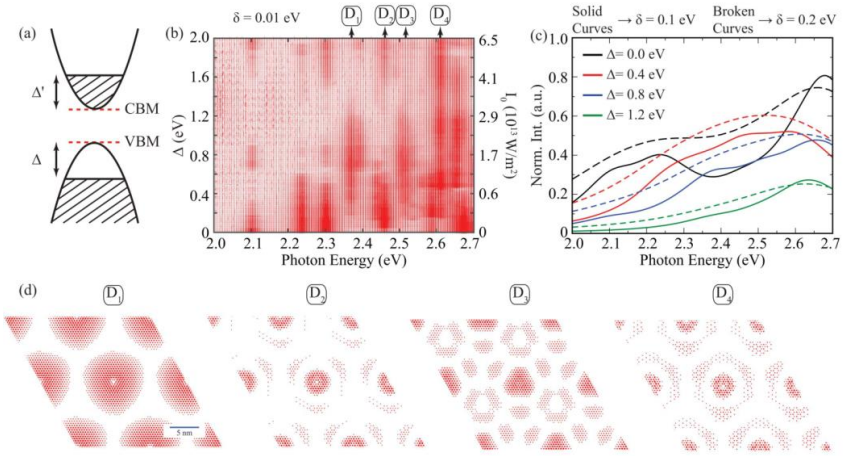

Figure 5.7. Theoretical interpretation of SHG modulation in monolayer MoS_2. (a), Schematic representation of the electronic bands of monolayer MoS_2 around the K-point, showing an effective depletion region Δ produced upon optical pumping, and a corresponding population of the conduction band up to an energy Δ′ adjusted to conserve the electron density. (b), Mapping of the oscillator strength of excitonic states in the vicinity of the optically active region as a function on photon energy and Δ. (c), Spectrally-resolved excitonic oscillator strength for Δ = 0, 0.4, 0.8, and 1.2 eV after introducing a photon energy broadening of 0.1 eV (solid curves) and 0.2 eV (broken curves). (d), Real-space wave functions of selected dark excitons, indicated by labels D1-D4 in b, respectively. Adapted from Publication 3.

To understand the observed optically-driven SHG enhancement, we elaborate a theoretical interpretation of our experimental results in monolayer MoS_2 based on first-principles calculations combined with a phenomenological treatment of optical pumping. We start by producing accurate calculations of the electronic band structure, as well as the exciton energies and wave functions. We then introduce optical pumping through an effective depletion of electrons within an energy interval Δ at the top of the valence band, accompanied by the corresponding filling near the bottom of the conduction band (Figure 5.7(a)). The optical transition strengths associated with the excitons are then modified by this redistribution of band occupations, which we directly introduce in the electron-hole-pair decomposition of their wave functions. This allows us to produce a map of exciton transition strengths resolved in photon energy and band depletion energy Δ (Figure 5.7(b)). Spectral variations for selected values of Δ are shown in Figure 5.7(c) after introducing a spectral broadening to facilitate comparison to the experiment. As the depletion energy increases, we find that the allowed excitations vary considerably: dark excitons with originally low oscillator strength increase their strength and dominate the optical spectrum, while bright excitons become weaker, in qualitative agreement with the experimental observations. We identify four dominant dark excitons in this process (D1-D4), whose real-space wave functions are plotted in Figure 5.7(d). In addition, assuming that all of the energy absorbed by the material from the control light is invested in producing a depletion Δ, we find that the required light intensities are a factor of ~3 lower than those used in the experiments (Figure 5.7(b), right scale), which is reasonable in view of the fact that part of that energy

can be lost in other dissipative processes (e.g., by spreading the energy among carriers away from the K point).

Table 5.1 Comparison of exciton energies in monolayer MoS_2.

Exciton	Ref. [225] (eV)	ΔP_{SHG} (eV)※	Linear reflection (eV)
$1s_A$	1.86	1.89	1.9
$3p_A$	2.13	-	-
$1s_B$	2.01	2.0	2.05
$2p_B$	2.22	2.27	-
$3p_B$	2.37	2.36	-
$1s_C$	-	2.9	2.93

※This work

Supported by these theoretical calculations, we attribute the SHG enhancement to the modified exciton oscillation strength created by a redistribution of excited carrier. In the enhancement region, we propose that some of the carriers in the quasi-continuum state excited by the control light scatter into low energy bands and modify the *e-h* composition of the excited dark excitonic states, which acquire a substantial transition strength, thus becoming bright and playing a leading role in SHG (Figure 5.5(b)). In consequence, we attribute the rise time (e.g., τ_0 = ~600 fs in Figure 5.4(b)) to the remorphing of the *e-h* pair composition of dark excitons. The enhancement decreases due to decay of the excited carrier states with a relatively slow bi-exponential behaviour (e.g., τ_1 = ~2.9 ps and τ_2 = ~325 ps at ~2.27 eV). We attribute the fast decay to cooling dynamics of the excited dark excitons, while the slow recovery can be related to carrier-phonon scattering and nonradiative carrier recombination. Note that the decay time in the enhancement region is typically ~10 times longer than the bi-exponential recovery components in the suppression region induced by bright excitons, which fits well with the results of excited exciton dynamics observed in previous experiments.[226] The leading role of dark excitons can be further confirmed by comparing the enhancement peak positions with calculated dark exciton results [77] and mid-infrared intra-band absorption measurements (details in Table 5.1).[225] We find that the two enhancement peaks at ~2.27 and ~2.36 eV are likely associated with the 2*p* and 3*p* excitonic states, respectively.

To explain the dynamics in the transition region, we plot time-resolved SHG modulation at different time delays in the ~2.5 to 2.6 eV spectral range as shown in Figure 5.8(a). The results confirm that the time-resolved SHG dynamics is governed by the contributions from the suppression and enhancement effects at different time scales: fast suppression process (<150 fs) in the transition region is initially dominated by bright exciton suppression, similar to the suppression region; then, a relatively slow (~1 ps) enhancement process takes over, similar to the initial response in the enhancement region. Such ultrashort response time allows ultrafast optical modulation. The response time can be measured with 20% to 80% of modulation with a rise (drop) time of 80 fs (900 fs), as shown in Figure 5.8 (b). It corresponds to a modulation speed of ~THz, which is much faster than state-of-the-art electro-optic modulators.[227] And the modulation depth is linearly dependent on the P_c and can be achieved as high as 62% when

P_c = 1.6 μW. The power consumption of P_c is calculated as 800 fJ, indicating a very low power consumption and high efficiency.

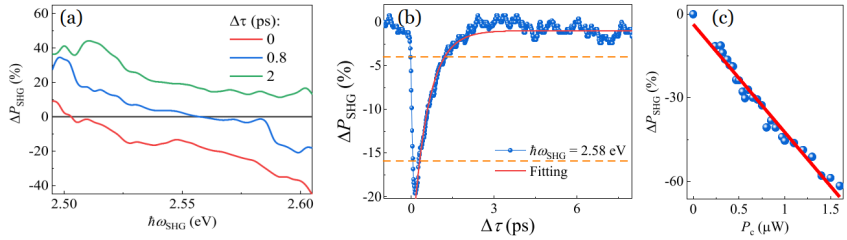

Figure 5.8. Ultrafast optical modulation. (a) ΔP_{SHG} spectra at different delays $\Delta\tau$. (b) ΔP_{SHG} with time delay when $\hbar\omega_{SHG}$ = 2.58 eV and P_c = 0.4 μW. (c) Power dependence of ΔP_{SHG} when $\Delta\tau$ = 0.15 ps. Adapted from Publication 3.

5.3 Transient second-harmonic generation in WS_2

We also carry out the SHG modulation in monolayer WS_2 with the same system to the one used for MoS_2 by using control light of 400 nm wavelength (3.1-eV photon energy). Monolayer WS_2 is grown by the CVD method similar to that with MoS_2.[228] Figure 5.9(a) shows the optical image of monolayer WS_2, exhibiting a typical triangular structure. The photoluminescence centred at 627 nm (1.98 eV) is measured by a 488-nm continuous laser, indicating the strong A exciton resonance (Figure 5.9(b)). And the reflection contrast measured by white light gives clear exciton states of A, B, C excitons at 627 nm (1.98 eV), 519 nm (2.39 eV), 394 nm (3.14 eV), as shown in Figure 5.9(c). Figure 5.9(d) gives the typical Raman shifts of WS_2, further confirming the good quality of the sample.

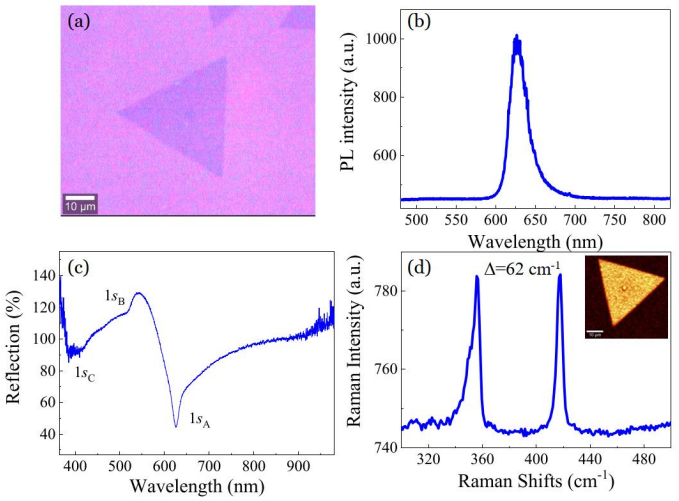

Figure 5.9. CVD WS_2 sample characterization. (a) Optical image. (b) Photoluminescence spectrum. (c) Optical reflectance. (d) Raman spectrum with an excitation wavelength of 488 nm. Inset: Raman map with the 336 cm^{-1} shift peak. Adapted from Publication 3.

Figure 5.10(a) shows the SHG power dependence on control light and seed light (1170 nm, 1.05 eV). The SHG enhancement factor γ increases with increasing control light power, whereas it decreases with increasing seed light power. Figure 5.10(b) shows γ as a function of control light power when the seed light power is 1 μW. It shows that γ can be as high as ~76 when the control light power is 0.3 μW.

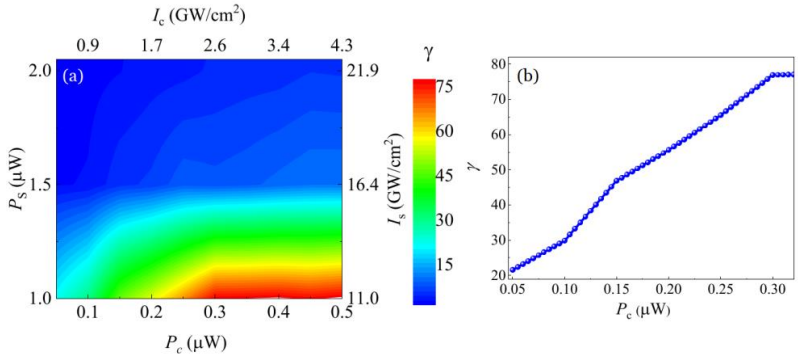

Figure 5.10. (a) SHG enhancement factor γ as a function of input power/peak-intensity of the control (P_c, I_c) and seed (P_s, I_s) light. (b) γ as a function of control light power for a seed light power of 1 μW. Adapted from Publication 3.

The normalized ΔP_{SHG} is shown in Figure 5.11(a) as a function of time delay at different seed light wavelengths. The incident average powers of the seed light and control light are ~3 μW and 0.3 μW, respectively. As shown in Figure 5.11(a), the time-resolved ΔP_{SHG} dynamics with various SHG energies clearly show suppression, transition, and enhancement regions. The SHG modulation results represented in Fig 5.11(b-e) show very similar dynamics when comparing the results of MoS_2 at different regions.

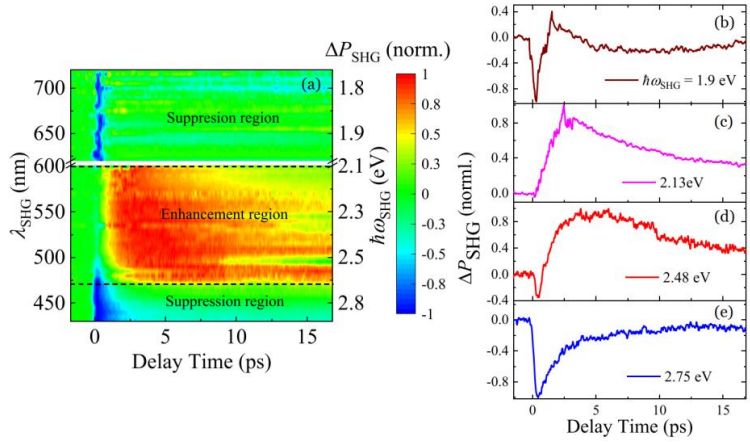

Figure 5.11. All-optical modulation dynamics in monolayer WS_2. (a) Normalized SHG power change ΔP_{SHG} as a function of time delay and SHG photon wavelength/energy. The breaking region signals the overlap between difference frequency generation and SHG. (b)-(e) ΔP_{SHG} dynamics when $\hbar\omega_{SHG}$ = 1.9, 2.13, 2.48, and 2.75 eV, respectively. Adapted from Publication 3.

Figure 5.12(a) shows ΔP_{SHG} results at a delay time of 2.8 ps. Comparing with the optical absorption results in Figure 5.12(b), we assign the dip at ~1.98 eV in the suppression region as the bright $1s_A$ state, which also matches well with the PL measurements. On the other hand, the enhancement region in the ΔP_{SHG} spectrum ranging from ~2.0 eV to 2.67 eV has a strong peak at ~2.11 eV and two small peaks at ~2.43 eV and ~2.58 eV, all of which are not visible in the linear inter-band absorption spectrum.

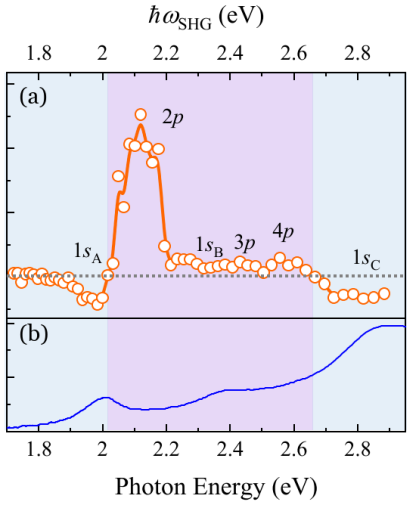

Figure 5.12. Maximum SHG modulation ΔP_{SHG} and optical absorption in monolayer MoS_2. (**a**) SHG change ΔP_{SHG} in monolayer WS_2 when $\Delta\tau$ = 2.8 ps, $\hbar\omega_c \approx$ 3.1 eV, $I_c \approx$ 2.57 GW/cm^2 and $I_s \approx$ 32.85 GW/cm^2. (b) Absorption spectrum of monolayer WS_2. Adapted from Publication 3.

The generality of the dark-exciton mechanism and the dynamics unveiled here is also supported by the SHG experiments with monolayer WS_2 (Figure 5.12). We could assign those peaks in the enhancement region as 2*p*, 3*p*, and 4*p* dark states, respectively, by comparing energies of dark states from reference [78,229]. Table 5.2 shows the comparison results. This suggests that all-optical modulation of SHG is indeed applicable to other TMDs as well as their heterostructures. We also note that similar modulation effects are possible in other nonlinear optical responses (e.g., third-harmonic generation, optical-comb generation, and high-harmonic generation), some of which will be discussed in the next chapter.

Table 5.2. Comparison of exciton energies in monolayer WS_2.

Unit: eV	$1s_A$	2*p*	$1s_B$	3*p*	4*p*	Temperature
Reference [78]	2.04	2.28	2.45	2.48		10k
Reference [229]	2.12	*	2.50	*	*	10k
Reference [229]	2.02	*	2.40	2.45	2.58	300k
Linear	1.98	*	2.39	*	*	300k
ΔP_{SHG}	1.98	2.11	*	2.43	2.58	300k

* unmeasured point.

6. Transient higher-order harmonic spectroscopy in MoS_2

Nonlinear optical spectroscopy has been widely utilized for the exploration of physical properties in various materials, such as semiconductors, metals, and bio-tissues. Besides SHG discussed in the last chapter, higher-order harmonic generations (HOHG), for example, THG in monolayer MoS_2 has been observed with relatively high conversion efficiency.[96,97,134,230] The strong nonlinear responses are contributed from vividly resonance enhancement, which can study electronic properties and thus play a complementary role in linear optical spectroscopy. The relation between HOHG and prominent carrier states (such as A, B, C excitons of monolayer TMDs) has been rarely studied.

In this chapter, we first demonstrate a broadband third-harmonic spectroscopy (THS) and transient THS ranging from ~1.77 to 3.10 eV in monolayer MoS_2 to explore prominent fingerprints of various electronic states and realize the efficient THG modulation with an optical method. The carrier dynamics at various states characterized by transient THS could offer a clear sign of carrier trajectories with exciton formation, electron-phonon interaction, and recombination in monolayer MoS_2. Further, we investigate the optical control of HHG in monolayer MoS_2 and achieve highly efficient HHG modulation at the atomic thickness.

6.1 Broadband third-harmonic generation

To observe the THG of monolayer MoS_2, we employ 150-fs laser pulses with the photon energy ranging from ~0.56 to 1.03 eV generated by an optical parametric amplifier (TOPAS) pumped with an 800-nm Ti:sapphire femtosecond laser. The fundamental pulses at $\hbar\omega_0$ are tightly focused on the sample by an objective lens (40×, 0.75 NA.), and the generated third-harmonic pulses at $\hbar\omega_{THG}$ are collected by the same objective, then reflected by a beam-splitter to the spectrometer. The full width at the half maximum of the excitation beam diameter on the sample is ~2.5 μm. Various polarizer and optical filters are used during the measurements. All the incident powers at different wavelengths are calibrated by a power meter behind the objective. All the experiments are performed at room temperature.

Figure 6.1(a) shows the diagram of THG in monolayer MoS_2 samples. Strong optical pulses with a photon energy of $\hbar\omega_0$ are incident onto the MoS_2 flake, generating pulses with a photon energy of $\hbar\omega_{THG}$ through the third-order optical

nonlinearity ($\chi^{(3)}$). A schematic plot of THG is shown in the up-right side of Figure 6.1(a). We tune the pulsed laser at ~0.79 eV with an average power of ~10 μW as the excitation source. The TH signal of monolayer MoS_2 on the sapphire substrate can be found around ~2.38 eV as shown in Figure 6.1(b). When gradually increasing the excitation power, the TH intensity grows with a power dependence of a slope of ~2.7 (Figure 6.1(c)). The dependence of THG on input/output polarization is uniform by rotating the azimuthal angle of the sample, which agrees with the structural symmetry of MoS_2, as shown in Figure 6.1(d). Note that all results here are measured under ambient conditions, and we do not observe the TH signal from the sapphire substrate under the same experimental conditions. This indicates that the third-order nonlinear susceptibility element $\chi^{(3)}$ of MoS_2 is responsible for the TH signal.

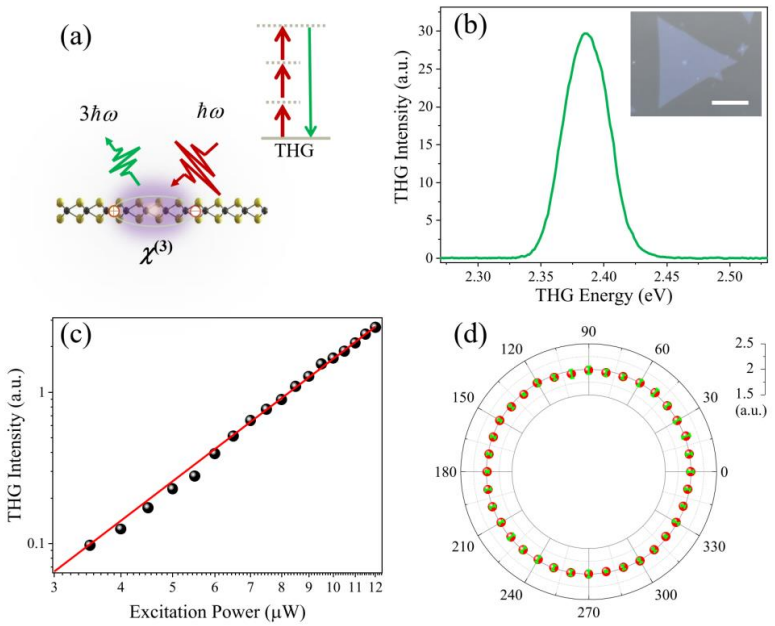

Figure 6.1. THG in monolayer MoS_2. (a) Schematic THG setup in monolayer MoS_2. Inset: energy level scheme of THG process. (b) THG spectrum. Inset: MoS_2 flake image. Scale bar 10 μm. (c) Power dependence and (d) Polarization dependence of TH signal. In Figures. (b-d), the excitation photon energy is ~0.79 eV. Adapted from Publication 4.

To quantify the strength of the third-harmonic signal of MoS_2, the effective third-order susceptibility $\chi^{(3)}$ was deduced by solving the coupled-wave equations when considering the MoS_2 sheet as a thin medium.[89,134] With the atomic thickness, the phase-matching and depletion of the fundamental beam are ignored during the THG process. Therefore, $|\chi^{(3)}_{eff}|$ is expressed as [45,89,96]

$$|\chi^{(3)}_{\mathrm{eff}}| = \frac{4\varepsilon_0 c^2}{3\omega d}\sqrt{n_\omega^3 n_{3\omega}\frac{I_{3\omega}}{I_\omega^3}} \qquad (6.1)$$

where ε_0 and c are the permittivity and speed of light in the vacuum, respectively. And ω, n_ω, I_ω and 3ω, $n_{3\omega}$, $I_{3\omega}$ are the frequency, refractive index, the peak

intensity of fundamental and TH pulses, respectively; $d \approx 0.65$ nm is the thickness of monolayer MoS_2. Here we use the value of $n_\omega = 3.5$, $n_{3\omega} = 4.6$ for the refractive indices at a photon energy of ~0.79 and ~2.38 eV.[231] When the excitation pulses is ~10 μW (peak power: ~141 GW/cm²), the power of TH signal is ~16 fW. Thus, we can obtain the value of $|\chi^{(3)}_{eff}|$ ~5×10^{-19} m²/V², similar to the previously measured third-order nonlinear susceptibilities (~10^{-19} m²/V² [98,134,230]).

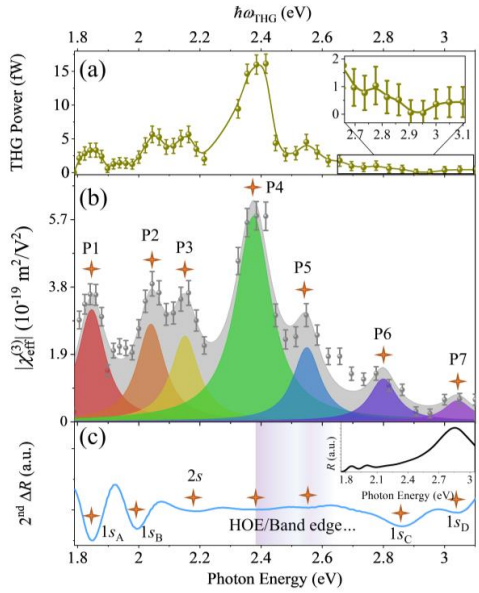

Figure 6.2. THS of monolayer MoS_2. (a) THG powers and (b) experimentally evaluated $\left|\chi^{(3)}_{eff}\right|$ as a function of THG photon energy, and (c) second-order linear reflectance derivation of monolayer MoS_2. Series peaks in (b) are labelled as P1-P7 by stars. Series electronic states (including exciton states) are labelled in (c). Adapted from Publication 4.

In order to carry out the broadband THS of monolayer MoS_2, ~150-fs incident fundamental pulses with photon energies ($\hbar\omega_0$) tunable from ~0.59 to 1.02 eV (λ_0: ~1210 to 2080 nm) are used to generate third-harmonic pulses. Figure 6.2(a) shows THG results at different incident wavelengths in monolayer MoS_2 with a fixed incident average power of ~10 μW (peak power: ~141 GW/cm²). The results show that THG signals are highly dependent on the incident fundamental wavelength. When $\hbar\omega_0$ is ~0.79 eV ($\lambda_0 \approx 1560$ nm), the THG ($\hbar\omega_{THG} \approx 2.37$ eV) efficiency is the highest compared to those at other incident photon energies. The variation of THG intensity efficiencies can reach ~800 times between ~1.79 eV and 3.08 eV, which shows remarkable THG enhancement at specific photon energies.[96]

To further understand the resonance peaks, we calculate the effective third-order nonlinear susceptibility $\left|\chi^{(3)}_{eff}\right|$ at different THG energies (the grey dots in Figure 6.2(b)). In Figure 6.2(b), the seven-resonant peaks (P1-P7) can be well fitted with the Lorentz function, where P1-P7 are located at ~1.84, 2.03, 2.16,

2.39, 2.55, 2.81, 3.05 eV, respectively. P4 is the strongest with $\left|\chi_{eff}^{(3)}\right|$ of ~5.7×10^{-19} m^2/V^2, which is comparable to previous results at the same wavelength region.[98,134]

In order to assign the observed peaks in the THS results, we extract the linear reflection spectrum into the second-order contrast derivative (Figure 6.2(c)). Seven dips have been observed, with photon energies of ~1.85, 2.00, 2.17, 2.38, 2.55, 2.84, and 3.05 eV, respectively. Interestingly, the THG peaks nicely match with the dips in the reflectance derivation spectrum, which gives strong evidence for the three-photon resonance of THG with electronic states. Among them, three dips in Figure 2(c) at ~1.85 eV, 2.00 eV, 2.84 eV obviously correspond to the A, B, C excitons with 1*s* series, matching THS peaks at P1, P2, P6 in Figure 6.2(b), respectively. This is similar to previously reported exciton enhanced SHG results in monolayer TMDs.[20,21] Then, we assign the dip at ~2.17 eV in Figure 6.2(c) and the corresponding Peak P3 (Figure 6.2(b)) to the 2*s* exciton.[83] The dip at ~2.38 eV in Figure 6.2(c), matching Peak P4 in Figure 6.2(b), possibly corresponds to the 3*s* exciton.[83] Meanwhile, P5 in Figure 6.2(b) and the corresponding weak dip at 2.55 eV in Figure 6.2(c) remain unknown to our current knowledge. The well-known band-nest effect contributes to the linear absorption at ~2.84 ($1s_C$), and 3.05 eV ($1s_D$), matching Peaks P6 and P7 in Figure 6.2(b). Thus far, all 7 electronic states of monolayer MoS_2 are nicely matching between linear absorption spectrum and THS (Table 6.1). With comparison with the linear reflection spectroscopy (Figure 6.2(c)), we can conclude that our THG method has advantages with high contrast (up to 800 times).

Still, there are two concerns that remained. One is that the THG at ~2.38 eV (P4) is extremely strong, in contrast to the weaker oscillation at high-order exciton states.[232] Also, the fitted FWHM width of Peak P4 in Figure 2(b) is ~0.14 eV, slightly larger than the other six peaks with a typical FWHM of ~0.11 eV. The substantial enhancement and broaden bandwidth possibly indicate additional resonance contribution to Peak P4, besides the 3*s* excitonic state. On the other hand, we find that the enhancement of the band-nesting (P6 and P7) on THG, is one order of magnitude smaller than that in linear and SHG responses.[20]

6.2 Transient third-harmonic generation

After gaining the knowledge of resonant enhanced THG, we carry out transient THS to study the carrier dynamics associated with the THG process, which is highly important for electronics and optoelectronics. Figure 6.3(a) shows the experimental setup of transient THS, which is similar to the transient SHG in Chapter 5. With the excitation of pump pulses at higher photon energy, carriers are excited to higher states and then relax to lower states (Figure 6.3(b)), resulting in the bleaching and then recovering of THG, offering a good way to identify the electronic states and relaxation dynamics. In our experiment, a pump light at ~3.1 eV is used with a delay line to adjust the time delay ($\Delta\tau$) between the

pump light and a wavelength-tunable seed light (i.e., the fundamental excitation pulses for THG).

Figure 6.3(c) shows the transient THG (ΔP_{THG}) at the generated photon energy of ~2.18 eV. The ΔP_{THG} is defined by the equation of $\Delta P_{THG}=(P_w - P_0)/P_w$, where P_w is the THG intensity with the pump excitation and P_0 is the THG intensity without the pump excitation. In Figure 6.3(c), when the pump pulses arrive, the THG intensity decreases quasi-instantaneously within ~100fs and reaches the lowest value of -88% at $\Delta\tau$ = ~0.3 ps. In the measurements, the pump excited carriers bleach the corresponding multi-photon transitions of THG, and thus decrease the THG efficiency.[233] Then, it begins to recover with a typical bi-exponential trajectory (the fitted time constants: a fast time constant of τ_1 = ~1.3 ps and a slow time constant of τ_2 = ~46.4 ps). It indicates two processes of carrier dynamics in the crystal lattice[234]: i) fast relaxation process: The pump excited carriers would decay from the continuum band to lower electronic states. Due to the relaxation of the hot carriers, the bleaching state steadily recovers. In this case, the multi-photon transition at exciton state is gradually built and the THG efficiency thus is recovered with the enhancement of exciton oscillations. This process usually happens within several picoseconds and is identified with a fast recovery time τ_1.[208,209,235] ii). Slow relaxation process. During this process, the interaction between the excited electron and phonon could play a key role, while other interactions from defect effects, charge trapping could also happen.[236,237]

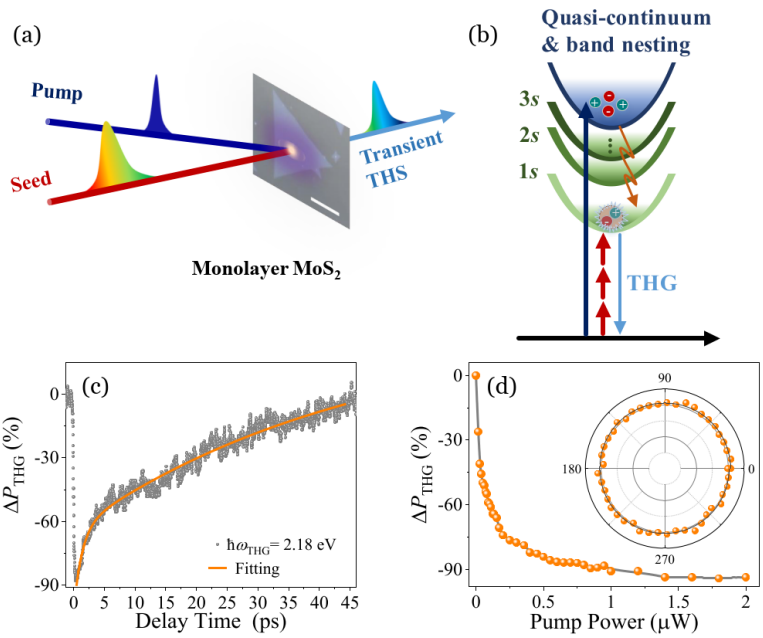

Figure 6.3. Transient THS of monolayer MoS_2. (a) Schematic illustration of transient THS; (b) illustration of carrier relaxation during transient THG process interacting with various electronic states, i.e., excitons. (c) Transient ΔP_{THG} when the seed and pump light powers are ~10 and 1 μW. The decay process is fitted by bi-exponential function (yellow

curve) with a fast time constant of ~1.3 ps and a slow time constant of ~46.4 ps. (d) ΔP_{THG} as a function of the pump power. Inset: polarization dependent ΔP_{THG}. Adapted from Publication 4.

By fixing the delay time ($\Delta\tau$) at ~0.3 ps and gradually increasing the pump power, we observe that ΔP_{THG} continuously decreases to -94% until the average pump power reaches ~1.8 μW (Figure 6.3(d)). The nonlinear behaviour of the power dependence could be explained by carrier depletion. The inset of Figure 6.3(d) shows the ΔP_{THG} as a function of the pump light polarization, indicating that the THG modulation is independent of the pump polarization.

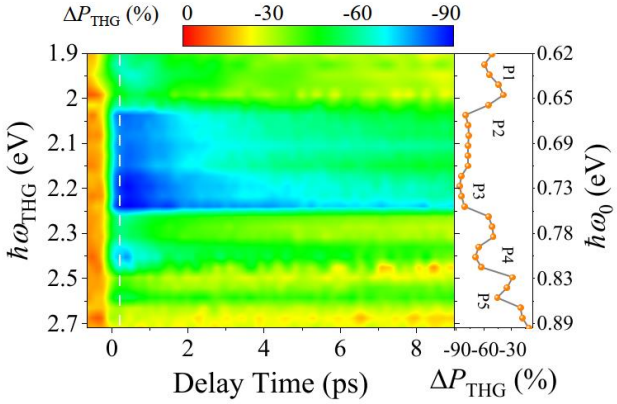

Figure 6.4. Transient THS at different $\hbar\omega_{THG}$ from ~1.9 to 2.7 eV; Right panel is the ΔP_{THG} at a delay time of ~0.2 ps. Adapted from Publication 4.

To find the relationship between electronic states and ΔP_{THG}, we collect the ΔP_{THG} by scanning the excitation seed energies from ~0.62 eV to ~0.89 eV (average seed light power: 10 μW) with ~1-μW pump pulses at ~3.1 eV (Figure 6.4). The results show that THG intensities decrease in the whole spectral region. Specifically, we extract the ΔP_{THG} response at the delay time $\Delta\tau$ = ~0.2 ps as shown in the right panel of Figure 6.4. It clearly shows five dips at ~1.87, 2.00, 2.18, 2.40, 2.55 eV respectively, which nicely agrees with the THS results (i.e., P1-P5) in Figure 6.2(b) and the reflectance spectrum in Figure 6.2(c) (Table 6.1). The ΔP_{THG} at C exciton (~2.8 eV) does not exhibit due to the weak THG signal. We find that the 2*s* state enhanced THG at Peak P3 enables the highest modulation depth, while that of the 3*s* state at Peak P4 is relatively weak. It possibly indicates that the electronic bandgap contribution to the THG enhancement at Peak P4, besides the higher-level excitonic states.

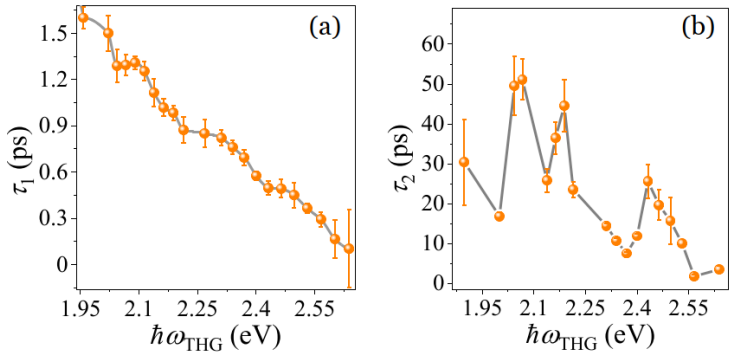

Figure 6.5. (a) Fast τ_1 and (b) slow τ_2 decay time constants as a function of THG photon energies. The grey lines in (a)-(b) are guides to eyes. Adapted from Publication 4.

Finally, we plot the fitted decay time constants as a function of the THG photon energy (Figure 6.5(a) and (b)). The fast time constant τ_1 decreases almost linearly with the THG photon energies from ~2.47 ps at ~1.88 eV to ~0.1 ps at ~2.64 eV. It is reasonable that it takes a longer time for lower energy exciton.[238] The slow time constant τ_2 does not show a clear linear relationship with THG photon energies, while it increases when the THG photon energy is close to the resonance states (i.e., $1s_B$ (P2), $2s$ (P3), $3s$ (P4)), as shown in Figure 6.5(b). This indicates that the bounded excitons have a longer lifetime.[239] With transient THS, various carrier dynamics can be monitored with high modulation depth (~90% in Figure 6.3(d)) and high resolution (<0.1ps in Figure 6.5(b)). Such a method could also be used for other TMDs and heterostructures to explore the dynamics of interlayer electronic states, such as moiré excitons.[240,241]

Table 6.1. Comparison of series of excitonic states.

Unit: eV	$1s_A$	$1s_B$	$2s$	$3s$	Electronic band	$1s_C$	$1s_D$
Reflectance	1.85	2.00	2.17	2.38	*	2.84	3.05
THG	1.84	2.03	2.16	2.39	2.55	2.81	3.05
Transient THG	1.87	2.00	2.18	2.40	2.55	*	*

6.3 Optical control of high-harmonic generation

High-harmonic generation (HHG) in solid materials [242], has attracted significant interest in the field of strong-field and attosecond physics. Since firstly observed in a bulk ZnO crystal in 2010 [149], solid-state HHG has been investigated with a wide range of materials, including large bandgap dielectrics [243] [244], semiconductors [151,245-247], semimetals [51], and topological insulators [248]. Along with optically modulated SHG and THG, the active control of the extreme nonlinear process would make a step forward to those potential applications. In this session, we investigate an optically controlled HHG in atomically thin 2D materials. The 2D materials with the advantages of strong optical nonlinearity and phase-matching-free have been found to motivate the essential

feature of HHG without propagation effects, thus take a unique role in extreme nonlinear optics.[51,138,246,249-251]

A monolayer MoS_2 flake employed in this experiment is the same with the previous sample grown by chemical vapor deposition (CVD) and its quality is confirmed by inspecting the photoluminescence and Raman spectroscopies (See Figure 4.1 in chapter 4). The nonlinear optical responses in monolayer MoS_2 are analysed at room temperature when illuminated with femtosecond seed pulses (~200 fs, 2 kHz, photon energy ~0.57 eV, See Figure 4.2). To control the nonlinear optical responses, we employ a control light with photon energy $\hbar\omega_c$ at ~3.1 eV. By tuning the delay time ($\Delta\tau$) between the control and seed pulses with a homemade delay line, the time-resolved HHG can be achieved.

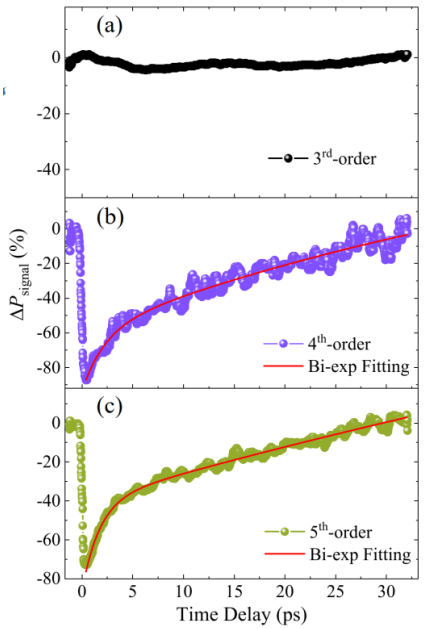

Figure 7.1. (a-c) Transient 3rd-, 4th-, 5th-HG signal in monolayer MoS_2 when the pump light energy is 3.1 eV with the average power 300 nW. The seed light photon energy is ~0.57 eV with an average power ~80 μW. Red curves are the bi-exponential fitting.

Figure 7.1 shows the ΔP_{signal} at the 3rd-, 4th-, 5th-harmonic photon energy as a function of delay time between the control and seed lights. In contrast to the previous results of transient THG, the 3rd-HG (i.e. THG) signal at 1.71 eV remains unchanged when the pump light arises. Note that the photon energy of 3rd-HG is lower than the energy of the optical bandgap (~1.8 eV). Thus, it is reasonable that there is no observable modulation at the 3rd-HG due to no resonance states. Whereas the 4th-HG at ~2.28 eV and 5th-HG at ~2.85 eV that are above the bandgap show efficient modulation with the pump light. For the 4th-HG, the ΔP_{4th} first decreases within ~100 fs due to the quasi-instantaneous optical bleaching, then the ΔP_{4th} starts to recover back. The bi-exponential fitting of the recovery trace gives a fast time constant of τ_1 ~2.2 ps and a slow time constant of τ_2 ~57.6 ps. The ΔP_{5th} behaves similarly to ΔP_{4th}, first decreasing

sharply within 100 fs and then recovering with bi-exponential time constants (τ_1 = ~1.7 ps, τ_2 = ~143.2 ps).

The underlying mechanism of solid-state HHG is generally described as an integration of interband transition and intraband oscillations.[7] Especially, when the photon energy of HHG is above the bandgap, the solid-state HHG operating with a significant overlap of atomic orbitals gives a rise of probability for the interband transition, which is applicable for explaining our experimental results.

7. Summary and outlook

In this thesis, we have systemically studied the light induced linear and nonlinear optical changes in 2D materials, specifically transient linear absorption, and harmonic generations with different order nonlinearities. During these processes, the excited carriers associated optical effects, such as exciton bleaching, formation, electron-phonon scattering, have been observed with an ultrafast time scale.

In chapter 4, we have studied the transient absorption of ML-MoS_2 in the NIR region from 0.86 to 1.4 μm and the achieved enhancement of absorption can be up to 4.2%. The time-resolved carrier dynamics with hundreds of femtosecond resolution provide detailed views of the relaxation time of the carriers. Furthermore, we observed that the absorption modulation amplitude is highly dependent on pump and probe intensities, due to the presence of excited carrier states with both one-photon and two-photon absorption processes.

In chapter 5, we have demonstrated giant all-optical modulation of SHG mediated by excitons in monolayer TMDs. The transient dynamics of excitonic dark and bright states in monolayer MoS_2 have been determined to be the origin of the observed SHG modulation. Thanks to a redistribution of charge carriers produced by a control light beam, excited states acquired a substantial transition strength that contributes to enhancing SHG by a factor as large as 386 in our measurements.

In chapter 6, we have demonstrated the high-contrast third-harmonic spectroscopy in monolayer MoS_2 and uncovered the various electronic states such as *s* series excitons and interlayer band-to-band transition effect. Furthermore, the carrier dynamics in monolayer MoS_2 have been vividly observed by highly sensitive transient THS with modulation depth up to 95%. Secondly, we have achieved the active controls of high-harmonic generation with the optical method in TMDs, indicating that the electronic state can also support the higher-order optical nonlinearity. Our optically controlled optical nonlinearity would pave a new route for the nonlinear optical engineering toward on-chip all-optical devices.

All in all, our results on all-optical modulations of linear absorption and harmonic generations provide a basis for exploiting the unique exciton-photon interactions in 2D materials, while they enable the development of emerging all-optical linear and nonlinear optoelectronic applications. For example, the modulation amplitude, sign, and response time in transient SHG can be adjusted

over a broad spectral range spanning a few eV's, which potentially enable versatile photonic devices with different functionalities. In particular, at a transition region, the large fractional SHG change $|\Delta P_{SHG}|$ (up to 62%) with the ultrafast rise (80 fs) and drop (~900 fs) response times could be used for ultrafast all-optical photonic devices, such as all-optical nonlinear modulators. Furthermore, the broadband transient linear and nonlinear responses provide a useful platform to explore the bright and dark excitons and related ultrafast dynamics. Benefited from all the features of 2DLMs, we believe that 2DLM-based nonlinear optics will pave the way for a wide variety of novel applications in various cross-disciplinary fields.

Thanks to the great progresses on nonlinear optics of 2D materials in the last decade [204], the basic nonlinear behaviours have been investigated in 2D materials and some methods of tunable nonlinear optics have been achieved. There still are plenty of opportunities to investigate fundamental physics and optoelectronic applications in 2D materials. For example, with atomic thickness, the nonlinear optical phenomena in 2D materials wouldn't be hindered by the phase matching and propagation effects such as self-phase modulation of excitation pulses, thus exhibits their intrinsic features. One possible scheme is that the investigation of HHG in 2D materials would give a better understanding to the debate about the physical mechanism of HHG.[7]

In addition, the twisted heterostructure has been investigated in the last decade, with amazing optoelectronic features of single-layer 2D materials.[252] Indeed, In 2018, Prof. Pablo Jarillo-Herrero's group has found that twisted bilayer graphene stacked at magic angle 1.1^{o} shows flat bands near-zero Fermi energy and exhibits superconductivity at 1.7 K.[253] The moiré excitons were then observed in van der Waals TMD heterostructures.[240,241,254,255] These discoveries give rise to the research on twistronics and launching a new study subject (e.g., linear and nonlinear optical behavior from moiré excitons) from 2D to 3D.[256-259]

References

[1] P. A. Franken, A. E. Hill, C. W. Peters and G. Weinreich, "Generation of Optical Harmonics," Physical Review Letters **7**, 118-119 (1961).

[2] X. Guo, C.-L. Zou and H. X. Tang, "Second-harmonic generation in aluminum nitride microrings with 2500%/W conversion efficiency," Optica **3**, 1126 (2016).

[3] F. Simon, S. Clevers, V. Dupray and G. Coquerel, "Relevance of the second harmonic generation to characterize crystalline samples," Chemical Engineering & Technology **38**, 971-983 (2015).

[4] W. R. Zipfel *et al.*, "Live tissue intrinsic emission microscopy using multiphoton-excited native fluorescence and second harmonic generation," Proceedings of the National Academy of Sciences **100**, 7075-7080 (2003).

[5] Y. R. Shen, "Surface properties probed by second-harmonic and sum-frequency generation," Nature **337**, 519 (1989).

[6] G. O. Clay *et al.*, "Spectroscopy of third-harmonic generation: evidence for resonances in model compounds and ligated hemoglobin," Journal Of the Optical Society Of America B-Optical Physics **23**, 932-950 (2006).

[7] S. Ghimire and D. A. Reis, "High-harmonic generation from solids," Nature Physics **15**, 10-16 (2018).

[8] M. Taghinejad and W. Cai, "All-optical Control of Light in Micro- and Nano-photonics," ACS Photonics **6**, 1082-1093 (2019).

[9] C. C. Chan. *Optical performance monitoring: advanced techniques for next-generation photonic networks*. (Academic Press, 2010).

[10] Y. Wang, K. D. Jöns and Z. Sun, "Integrated photon-pair sources with nonlinear optics," Applied Physics Reviews **8**, 011314 (2021).

[11] R. B. Davidson *et al.*, "Ultrafast plasmonic control of second harmonic generation," ACS Photonics **3**, 1477-1481 (2016).

[12] J. C. Johnson *et al.*, "Ultrafast carrier dynamics in single ZnO nanowire and nanoribbon lasers," Nano Letters **4**, 197-204 (2004).

[13] A. McClelland, V. Fomenko and E. Borguet, "Ultrafast hot-carrier dynamics at chemically modified Ge interfaces probed by SHG," Journal Of Physical Chemistry B **110**, 19784-19787 (2006).

[14] W. A. Tisdale *et al.*, "Hot-electron transfer from semiconductor nanocrytal," Science **328**, 1543-1547 (2010).

[15] A. E. Jailaubekov *et al.*, "Hot charge-transfer excitons set the time limit for charge separation at donor/acceptor interfaces in organic photovoltaics," Nature Materials **12**, 66-73 (2013).

[16] X. Duan *et al.*, "Two-dimensional transition metal dichalcogenides as atomically thin semiconductors: opportunities and challenges," Chemical Society Review **44**, 8859-8876 (2015).

[17] K. F. Mak and J. Shan, "Photonics and optoelectronics of 2D semiconductor transition metal dichalcogenides," Nature Photonics **10**, 216-226 (2016).

[18] R. R. Nair *et al.*, "Fine structure constant defines visual transparency of graphene," Science **320**, 1308 (2008).

[19] E. Hendry *et al.*, "Coherent nonlinear optical response of graphene," Physics Review Letters **105**, 097401 (2010).

[20] L. M. Malard *et al.*, "Observation of intense second harmonic generation from MoS_2 atomic crystals," Physical Review B **87**, 201401 (2013).

[21] G. Wang *et al.*, "Giant enhancement of the optical second-harmonic emission of WSe_2 monolayers by laser excitation at exciton resonances," Physical Review Letters **114**, 097403 (2015).

[22] N. Kumar *et al.*, "Second harmonic microscopy of monolayer MoS_2," Physical Review B **87**, 161403 (2013).
[23] J. Xiao, M. Zhao, Y. Wang and X. Zhang, "Excitons in atomically thin 2D semiconductors and their applications," Nanophotonics **0**, 1309-1328 (2017).
[24] G. Wang *et al.*, "Colloquium: Excitons in atomically thin transition metal dichalcogenides," Reviews of Modern Physics **90**, 021001 (2018).
[25] K.-Q. Lin, S. Bange and J. M. Lupton, "Quantum interference in second-harmonic generation from monolayer WSe_2," Nature Physics **15**, 242-246 (2019).
[26] Y. Wang *et al.*, "All-optical control of microfiber resonator by graphene's photothermal effect," Applied Physics Letters **108**, 171905 (2016).
[27] X. Gan *et al.*, "Graphene-assisted all-fiber phase shifter and switching," Optica **2**, 468 (2015).
[28] A. K. Geim and K. S. Novoselov, "The rise of graphene," Nature Materials **6**, 183-191 (2007).
[29] A. C. Ferrari *et al.*, "Science and technology roadmap for graphene, related two-dimensional crystals, and hybrid systems," Nanoscale **7**, 4598-4810 (2015).
[30] Y. Liu *et al.*, "Promises and prospects of two-dimensional transistors," Nature **591**, 43-53 (2021).
[31] T. H. Zhipei Sun, Francesco Bonaccorso, Felice Torrisi, Denis M. Basko, Daniel Popa, Andrea C. Ferrari, "Graphene Mode-Locked Ultrafast Laser," ACS Nano **4**, 803-810 (2010).
[32] F. H. Koppens *et al.*, "Photodetectors based on graphene, other two-dimensional materials and hybrid systems," Nature Nanotechnology **9**, 780-793 (2014).
[33] J. R. Schaibley *et al.*, "Valleytronics in 2D materials," Nature Reviews Materials **1**, 1-15 (2016).
[34] A. H. Castro Neto *et al.*, "The electronic properties of graphene," Reviews of Modern Physics **81**, 109-162 (2009).
[35] K. S. Novoselov *et al.*, "Two-dimensional gas of massless Dirac fermions in graphene," Nature **438**, 197-200 (2005).
[36] S. V. Morozov *et al.*, "Giant intrinsic carrier mobilities in graphene and its bilayer," Physical Review Letters **100**, 016602 (2008).
[37] E. Gruber *et al.*, "Ultrafast electronic response of graphene to a strong and localized electric field," Nature Communications **7**, 13948 (2016).
[38] B. Jalali and S. Fathpour, "Silicon photonics," Journal Of Lightwave Technology **24**, 4600-4615 (2006).
[39] K. F. Mak, J. Shan and T. F. Heinz, "Seeing Many-Body Effects in Single- and Few-Layer Graphene: Observation of Two-Dimensional Saddle-Point Excitons," Physical Review Letters **106**, 046401 (2011).
[40] D. Li *et al.*, "Graphene actively Q-switched lasers," 2D Materials **4**, 025095 (2017).
[41] M. Breusing *et al.*, "Ultrafast nonequilibrium carrier dynamics in a single graphene layer," Physical Review B **83**, 153410 (2011).
[42] A. Tomadin *et al.*, "The ultrafast dynamics and conductivity of photoexcited graphene at different Fermi energies," Science advances **4**, eaar5313 (2018).
[43] X. Gan *et al.*, "Graphene-controlled fiber Bragg grating and enabled optical bistability," Optics Letters **41**, 603-606 (2016).
[44] A. Saynatjoki *et al.*, "Rapid Large-Area Multiphoton Microscopy for Characterization of Graphene," ACS Nano **7**, 8441-8446 (2013).
[45] N. Kumar *et al.*, "Third harmonic generation in graphene and few-layer graphite films," Physical Review B **87**, 121406(R) (2013).
[46] S.-Y. Hong *et al.*, "Optical Third-Harmonic Generation in Graphene," Physical Review X **3**, 021014 (2013).
[47] T. Gu *et al.*, "Regenerative oscillation and four-wave mixing in graphene optoelectronics," Nature Photonics **6**, 554 (2012).
[48] N. Vermeulen *et al.*, "Negative Kerr nonlinearity of graphene as seen via chirped-pulse-pumped self-phase modulation," Physical Review Applied **6**, 044006 (2016).
[49] R. Wu *et al.*, "Purely Coherent Nonlinear Optical Response in Solution Dispersions of Graphene Sheets," Nano Letters **11**, 5159-5164 (2011).
[50] N. Vermeulen *et al.*, "Graphene's nonlinear-optical physics revealed through exponentially growing self-phase modulation," Nature Communications **9**, 2675 (2018).
[51] N. Yoshikawa, T. Tamaya and K. Tanaka, "High-harmonic generation in graphene enhanced by elliptically polarized light excitation," Science **356**, 736-738 (2017).

[52] H. A. Hafez *et al.*, "Extremely efficient terahertz high-harmonic generation in graphene by hot Dirac fermions," Nature **561**, 507-511 (2018).
[53] J. Wang *et al.*, "Broadband Nonlinear Optical Response of Graphene Dispersions," Advanced Materials **21**, 2430-2435 (2009).
[54] H. Zhang *et al.*, "Z-scan measurement of the nonlinear refractive index of graphene," Optics letters **37**, 1856-1858 (2012).
[55] H. Yang *et al.*, "Giant Two-Photon Absorption in Bilayer Graphene," Nano Letters **11**, 2622–2627 (2011).
[56] G. Bai *et al.*, "2D Layered Materials of Rare-Earth Er-Doped MoS_2 with NIR-to-NIR Down- and Up-Conversion Photoluminescence," Advanced Materials **28**, 7472-7477 (2016).
[57] J. L. Cheng, N. Vermeulen and J. E. Sipe, "Second order optical nonlinearity of graphene due to electric quadrupole and magnetic dipole effects," Scientific Reports **7**, 43843 (2017).
[58] Y. Zhang *et al.*, "Doping-Induced Second-Harmonic Generation in Centrosymmetric Graphene from Quadrupole Response," Physical Review Letters **122**, 047401 (2019).
[59] S. J. Brun and T. G. Pedersen, "Intense and tunable second-harmonic generation in biased bilayer graphene," Physical Review B **91**, 205405 (2015).
[60] Y. Q. An, F. Nelson, J. U. Lee and A. C. Diebold, "Enhanced Optical Second-Harmonic Generation from the Current-Biased Graphene/SiO_2/Si(001) Structure," Nano Letters **13**, 2104-2109 (2013).
[61] S. Wu *et al.*, "Electrical tuning of valley magnetic moment through symmetry control in bilayer MoS_2," Nature Physics **9**, 149-153 (2013).
[62] F. Bonaccorso *et al.*, "Production and processing of graphene and 2d crystals," Materials Today **15**, 564-589 (2012).
[63] G. Soavi *et al.*, "Broadband, electrically tunable third-harmonic generation in graphene," Nature Nanotechnology **13**, 583-588 (2018).
[64] T. Jiang *et al.*, "Gate-tunable third-order nonlinear optical response of massless Dirac fermions in graphene," Nature Photonics **12**, 430-436 (2018).
[65] K. Alexander *et al.*, "Electrically Tunable Optical Nonlinearities in Graphene-Covered SiN Waveguides Characterized by Four-Wave Mixing," ACS Photonics **4**, 3039-3044 (2017).
[66] E. J. Lee *et al.*, "Active control of all-fibre graphene devices with electrical gating," Nature Communications **6**, 6851 (2015).
[67] F. Bonaccorso, Z. Sun, T. Hasan and A. C. Ferrari, "Graphene photonics and optoelectronics," Nature Photonics **4**, 611-622 (2010).
[68] F. Bo *et al.*, "Broadband Graphene Saturable Absorber for Pulsed Fiber Lasers at 1, 1.5, and 2 um," Ieee Journal of Selected Topics in Quantum Electronics **20**, 411-415 (2014).
[69] A. Martinez and Z. Sun, "Nanotube and graphene saturable absorbers for fibre lasers," Nature Photonics **7**, 842-845 (2013).
[70] Z. Sun, A. Martinez and F. Wang, "Optical modulators with 2D layered materials," Nature Photonics **10**, 227-238 (2016).
[71] U. J. n. Keller, "Recent developments in compact ultrafast lasers," Nature **424**, 831-838 (2003).
[72] J. Bogusławski *et al.*, "Graphene actively mode-locked lasers," Advanced Functional Materials **28**, 1801539 (2018).
[73] D. Li *et al.*, "Active synchronization and modulation of fiber lasers with a graphene electro-optic modulator," Optics letters **43**, 3497-3500 (2018).
[74] Y. Wang *et al.*, "All-optically controlled slow and fast lights in graphene-coated tilted fiber Bragg grating," Applied Physics Express **12**, 072010 (2019).
[75] C. T. Phare, Y. H. D. Lee, J. Cardenas and M. Lipson, "Graphene electro-optic modulator with 30 GHz bandwidth," Nature Photonics **9**, 511 (2015).
[76] K. F. Mak *et al.*, "Atomically thin MoS_2: a new direct-gap semiconductor," Physics Review Letters **105**, 136805 (2010).
[77] D. Y. Qiu, F. H. da Jornada and S. G. Louie, "Optical spectrum of MoS_2: many-body effects and diversity of exciton states," Physics Review Letters **111**, 216805 (2013).
[78] Z. Ye *et al.*, "Probing excitonic dark states in single-layer tungsten disulphide," Nature **513**, 214-218 (2014).
[79] Z. Y. Zhu, Y. C. Cheng and U. Schwingenschlogl, "Giant spin-orbit-induced spin splitting in two-dimensional transition-metal dichalcogenide semiconductors," Physical Review B **84**, 153402 (2011).

[80] J. A. Miwa *et al.*, "Electronic Structure of Epitaxial Single-Layer MoS_2," Physical Review Letters **114**, 046802 (2015).
[81] H. M. Hill *et al.*, "Band Alignment in MoS_2/WS_2 Transition Metal Dichalcogenide Heterostructures Probed by Scanning Tunneling Microscopy and Spectroscopy," Nano Letters **16**, 4831-4837 (2016).
[82] A. Chernikov *et al.*, "Population inversion and giant bandgap renormalization in atomically thin WS_2 layers," Nature Photonics **9**, 466 (2015).
[83] H. M. Hill *et al.*, "Observation of Excitonic Rydberg States in Monolayer MoS_2 and WS_2 by Photoluminescence Excitation spectroscopy," Nano Letters **15**, 2992-2997 (2015).
[84] A. Molina-Sanchez *et al.*, "Effect of spin-orbit interaction on the optical spectra of single-layer, double-layer, and bulk MoS_2," Physical Review B **88**, 045412 (2013).
[85] O. Lopez-Sanchez *et al.*, "Ultrasensitive photodetectors based on monolayer MoS_2," Nature Nanotechnology **8**, 497-501 (2013).
[86] H. Xue *et al.*, "A $MoSe_2/WSe_2$ heterojunction-based photodetector at telecommunication wavelengths," Advanced Functional Materials **28**, 1804388 (2018).
[87] G. F. Rao *et al.*, "Two-dimensional heterostructure promoted infrared photodetection devices," InfoMat **1**, 272-288 (2019).
[88] Y. R. Shen. *The principles of nonlinear optics*. (1984).
[89] R. W.Boyd. *Nonlinear Optics*. (2007).
[90] T. F. Heinz. in *Nonlinear surface electromagnetic phenomena* (ed H. E. and Stegeman Ponath, G. I.) Ch. 5, (Elsevier Science, 1991).
[91] J. J. Dean and H. M. van Driel, "Second harmonic generation from graphene and graphitic films," Applied Physics Letters **95**, 261910 (2009).
[92] Y. Li *et al.*, "Probing symmetry properties of few-layer MoS_2 and h-BN by optical second-harmonic generation," Nano Letters **13**, 3329-3333 (2013).
[93] L. Malard *et al.*, "Observation of intense second harmonic generation from MoS_2 atomic crystals," Physical Review B **87**, 201401 (2013).
[94] L. Mennel *et al.*, "Band nesting in two-dimensional crystals: An exceptionally sensitive probe of strain," Nano Letters **20**, 4242-4248 (2020).
[95] Y. W. Ho *et al.*, "Measuring Valley Polarization in Two-Dimensional Materials with Second-Harmonic Spectroscopy," ACS Photonics **7**, 925-931 (2020).
[96] R. Wang *et al.*, "Third-harmonic generation in ultrathin films of MoS_2," ACS Applied Materials Interfaces **6**, 314-318 (2014).
[97] R. I. Woodward *et al.*, "Characterization of the second- and third-order nonlinear optical susceptibilities of monolayer MoS_2 using multiphoton microscopy," 2D Materials **4**, 011006 (2016).
[98] L. Karvonen *et al.*, "Rapid visualization of grain boundaries in monolayer MoS_2 by multiphoton microscopy," Nature Communications **8**, 15714 (2017).
[99] A. Säynätjoki *et al.*, "Ultra-strong nonlinear optical processes and trigonal warping in MoS_2 layers," Nature Communications **8**, 893 (2017).
[100] A. Autere *et al.*, "Rapid and large-area characterization of exfoliated black phosphorus using third-harmonic generation microscopy," The Journal of Physical Chemistry Letters **8**, 1343-1350 (2017).
[101] N. Youngblood *et al.*, "Layer Tunable Third-Harmonic Generation in Multilayer Black Phosphorus," ACS Photonics **4**, 8-14 (2016).
[102] M. J. Rodrigues *et al.*, "Resonantly Increased Optical Frequency Conversion in Atomically Thin Black Phosphorus," Advanced Materials **28**, 10693-10700 (2016).
[103] J. Ribeiro-Soares *et al.*, "Second Harmonic Generation in WSe_2," 2D Materials **2**, 045015 (2015).
[104] H. Zeng *et al.*, "Optical signature of symmetry variations and spin-valley coupling in atomically thin tungsten dichalcogenides," Scientific Reports **3**, 1608 (2013).
[105] C. Janisch *et al.*, "Extraordinary Second Harmonic Generation in Tungsten Disulfide Monolayers," Scientific Reports **4**, 5530 (2014).
[106] H. Zeng *et al.*, "Optical signature of symmetry variations and spin-valley coupling in atomically thin tungsten dichalcogenides," Scientific Reports **3**, 1608 (2013).
[107] X. Lin *et al.*, "Two-Dimensional Pyramid-like WS_2 Layered Structures for Highly Efficient Edge Second-Harmonic Generation," ACS Nano **12**, 689-696 (2018).
[108] X. Fan *et al.*, "Mechanism of Extreme Optical Nonlinearities in Spiral WS_2 above the Bandgap," Nano Letters **20**, 2667-2673 (2020).
[109] C. T. Le *et al.*, "Impact of selenium doping on resonant second harmonic generation in monolayer MoS_2," ACS Photonics **4**, 38-44 (2017).

[110] C. T. Le *et al.*, "Nonlinear optical characteristics of monolayer $MoSe_2$," Annalen der Physik **528**, 551-559 (2016).
[111] L. Karvonen *et al.*, "Investigation of Second- and Third-Harmonic Generation in Few-Layer Gallium Selenide by Multiphoton Microscopy," Scientific Reports **5**, 10334 (2015).
[112] W. Jie *et al.*, "Layer-dependent nonlinear optical properties and stability of non-centrosymmetric modification in few-layer GaSe sheets," Angewandte Chemie **54**, 1185-1189 (2015).
[113] X. Zhou *et al.*, "Strong Second-Harmonic Generation in Atomic Layered GaSe," Journal of the American Chemical Society **137**, 7994-7997 (2015).
[114] Y. Tang, K. C. Mandal, J. A. McGuire and C. W. Lai, "Layer- and frequency-dependent second harmonic generation in reflection from GaSe atomic crystals," Physical Review B **94** (2016).
[115] X.-T. Gan *et al.*, "Microwatts continuous-wave pumped second harmonic generation in few- and mono-layer GaSe," Light: Science & Applications **7**, 17126 (2018).
[116] J. Susoma *et al.*, "Second and third harmonic generation in few-layer gallium telluride characterized by multiphoton microscopy," Applied Physics Letters **108**, 073103 (2016).
[117] A. A. Popkova *et al.*, "Optical Third-Harmonic Generation in Hexagonal Boron Nitride Thin Films," ACS Photonics **8**, 824-831 (2021).
[118] C.-J. Kim *et al.*, "Stacking Order Dependent Second Harmonic Generation and Topological Defects in h-BN Bilayers," Nano Letters **13**, 5660-5665 (2013).
[119] S. H. Rhim, Y. S. Kim and A. J. Freeman, "Strain-induced giant second-harmonic generation in monolayered 2H-MoX_2 (X = S, Se, Te)," Applied Physics Letters **107**, 241908 (2015).
[120] R. Beams *et al.*, "Characterization of Few-Layer 1T' $MoTe_2$ by Polarization-Resolved Second Harmonic Generation and Raman Scattering," ACS Nano **10**, 9626-9636 (2016).
[121] Y. Song *et al.*, "Second Harmonic Generation in Atomically Thin $MoTe_2$," Advanced Optical Materials **6**, 1701334 (2018).
[122] S. Deckoff-Jones *et al.*, "Observing the interplay between surface and bulk optical nonlinearities in thin van der Waals crystals," Scientific Reports **6**, 22620 (2016).
[123] Q. Cui, R. A. Muniz, J. E. Sipe and H. Zhao, "Strong and anisotropic third-harmonic generation in monolayer and multilayer ReS_2," Physical Review B **95**, 165406 (2017).
[124] Z. Sun *et al.*, "Giant nonreciprocal second-harmonic generation from antiferromagnetic bilayer CrI_3," Nature **572**, 497-501 (2019).
[125] X. Wang *et al.*, "Second-harmonic generation in quaternary atomically thin layered $AgInP_2S_6$ crystals," Applied Physics Letters **109**, 123103 (2016).
[126] C. Janisch *et al.*, "Ultrashort optical pulse characterization using WS_2 monolayers," Optics Letters **39**, 383-385 (2014).
[127] B. Xu, A. Martinez and S. Yamashita, "Mechanically Exfoliated Graphene for Four-Wave-Mixing-Based Wavelength Conversion," Ieee Photonics Technology Letters **24**, 1792-1794 (2012).
[128] S. Yamashita, "A Tutorial on Nonlinear Photonic Applications of Carbon Nanotube and Graphene," Journal of Lightwave Technology **30**, 427-447 (2012).
[129] Y. Li *et al.*, "Probing symmetry properties of few-layer MoS_2 and h-BN by optical second-harmonic generation," Nano Letters **13**, 3329 (2013).
[130] C. R. Dean *et al.*, "Boron nitride substrates for high-quality graphene electronics," Nature Nanotechnology **5**, 722-726 (2010).
[131] J. Klein *et al.*, "Electric-field switchable second-harmonic generation in bilayer MoS_2 by inversion symmetry breaking," Nano Letters **17**, 392−398 (2017).
[132] H. Yu *et al.*, "Charge-induced second-harmonic generation in bilayer WSe_2," Nano Letters **15**, 5653-5657 (2015).
[133] X. Fan *et al.*, "Broken Symmetry Induced Strong Nonlinear Optical Effects in Spiral WS_2 Nanosheets," ACS Nano **11**, 4892-4898 (2017).
[134] A. Saynatjoki *et al.*, "Ultra-strong nonlinear optical processes and trigonal warping in MoS_2 layers," Nature Communications **8**, 893 (2017).
[135] D. J. Clark *et al.*, "Near bandgap second-order nonlinear optical characteristics of MoS_2 monolayer transferred on transparent substrates," Applied Physics Letters **107**, 131113 (2015).

[136] K. L. Seyler *et al.*, "Electrical control of second-harmonic generation in a WSe_2 monolayer transistor," Nature Nanotechnology **10**, 407-411 (2015).
[137] W. T. Hsu *et al.*, "Second harmonic generation from artificially stacked transition metal dichalcogenide twisted bilayers," ACS Nano **8**, 2951-2958 (2014).
[138] H. Liu *et al.*, "High-harmonic generation from an atomically thin semiconductor," Nature Physics **13**, 262-265 (2016).
[139] J. L. Cheng, N. Vermeulen and J. E. Sipe, "Third order optical nonlinearity of graphene," New Journal of Physics **16**, 053014 (2014).
[140] C.-C. Lee, J. M. Miller and T. R. Schibli, "Doping-induced changes in the saturable absorption of monolayer graphene," Applied Physics B **108**, 129-135 (2012).
[141] H. Shi *et al.*, "Tuning the nonlinear optical absorption of reduced graphene oxide by chemical reduction," Optics Express **22**, 19375-19385 (2014).
[142] J. Zeng *et al.*, "Enhanced second harmonic generation of MoS_2 layers on a thin gold film," Nanoscale **7**, 13547-13553 (2015).
[143] H. Nan *et al.*, "Strong Photoluminescence Enhancement of MoS_2 through Defect Engineering and Oxygen Bonding," ACS Nano **8**, 5738–5745 (2014).
[144] J. Liang *et al.*, "Universal imaging of full strain tensor in 2D crystals with third-harmonic generation," Advanced Materials **31**, 1808160 (2019).
[145] F. Krausz and M. Ivanov, "Attosecond physics," Reviews of Modern Physics **81**, 163-234 (2009).
[146] C. Hernandez-Garcia *et al.*, "Zeptosecond High Harmonic keV X-Ray Waveforms Driven by Midinfrared Laser Pulses," Physical Review Letters **111**, 033002 (2013).
[147] T. Popmintchev *et al.*, "The attosecond nonlinear optics of bright coherent X-ray generation," Nature Photonics **4**, 822-832 (2010).
[148] A. McPherson *et al.*, "Studies of multiphoton production of vacuum-ultraviolet radiation in the rare gases," Journal of the Optical Society of America B **4**, 595-601 (1987).
[149] S. Ghimire *et al.*, "Observation of high-order harmonic generation in a bulk crystal," Nature Physics **7**, 138-141 (2010).
[150] M. Hohenleutner *et al.*, "Real-time observation of interfering crystal electrons in high-harmonic generation," Nature **523**, 572-575 (2015).
[151] N. Yoshikawa *et al.*, "Interband resonant high-harmonic generation by valley polarized electron-hole pairs," Nature Communications **10**, 3709 (2019).
[152] P. G. Hawkins *et al.* in *Conference on Lasers and Electro-Optics*. FM3D.7 (Optical Society of America).
[153] I. Al-Naib, J. E. Sipe and M. M. Dignam, "High harmonic generation in undoped graphene: Interplay of inter- and intraband dynamics," Physical Review B **90**, 245423 (2014).
[154] F. Langer *et al.*, "Lightwave-driven quasiparticle collisions on a subcycle timescale," Nature **533**, 225-229 (2016).
[155] S. Uddin, P. C. Debnath, K. Park and Y.-W. Song, "Nonlinear Black Phosphorus for Ultrafast Optical Switching," Scientific Reports **7**, 43371 (2017).
[156] D. A. Li *et al.*, "Polarization and Thickness Dependent Absorption Properties of Black Phosphorus: New Saturable Absorber for Ultrafast Pulse Generation," Scientific Reports **5**, 15899 (2015).
[157] A. Allain, J. Kang, K. Banerjee and A. Kis, "Electrical contacts to two-dimensional semiconductors," Nature Materials **14**, 1195-1205 (2015).
[158] X. Wu and L. Tong, "Optical microfibers and nanofibers," Nanophotonics **2**, 407 (2013).
[159] Y. Wu *et al.*, "Generation of cascaded four-wave-mixing with graphene-coated microfiber," Photonics Research **3**, A64-A68 (2015).
[160] U. Keller, "Recent developments in compact ultrafast lasers," Nature **424**, 831-838 (2003).
[161] L. Guo *et al.*, "Diode-end-pumped passively mode-locked ceramic Nd : YAG Laser with a semiconductor saturable mirror," Optics Express **13**, 4085-4089 (2005).
[162] R. L. Sutherland. *Handbook of Nonlinear Optics*. 2 edn, (2003).
[163] Z. Sun *et al.*, "Graphene Mode-Locked Ultrafast Laser," ACS Nano **4**, 803-810 (2010).
[164] Q. Bao *et al.*, "Atomic-Layer Graphene as a Saturable Absorber for Ultrafast Pulsed Lasers," Advanced Functional Materials **19**, 3077-3083 (2009).
[165] T. Hasan *et al.*, "Nanotube-Polymer Composites for Ultrafast Photonics," Advanced Materials **21**, 3874-3899 (2009).

[166] Z. Sun, T. Hasan and A. C. Ferrari, "Ultrafast lasers mode-locked by nanotubes and graphene," Physica E **44**, 1082-1091 (2012).
[167] K. P. Wang *et al.*, "Ultrafast Saturable Absorption of Two-Dimensional MoS_2 Nanosheets," ACS Nano **7**, 9260-9267 (2013).
[168] F. Bonaccorso and Z. Sun, "Solution processing of graphene, topological insulators and other 2d crystals for ultrafast photonics," Optical Materials Express **4**, 63 (2013).
[169] R. Woodward *et al.*, "Tunable Q-switched fiber laser based on saturable edge-state absorption in few-layer molybdenum disulfide (MoS_2)," Optics Express **22**, 31113-31122 (2014).
[170] Y. Huang *et al.*, "Widely-tunable, passively Q-switched erbium-doped fiber laser with few-layer MoS_2 saturable absorber," Optics Express **22**, 25258-25266 (2014).
[171] H. Zhang *et al.*, "Molybdenum disulfide (MoS_2) as a broadband saturable absorber for ultra-fast photonics," Optics Express **22**, 7249-7260 (2014).
[172] Z. Luo *et al.*, "Two-dimensional materials saturable absorbers: Towards compact visible-wavelength all-fiber pulsed lasers," Nanoscale **8**, 1066-1072 (2016).
[173] S. F. Zhang *et al.*, "Direct Observation of Degenerate Two-Photon Absorption and Its Saturation in WS_2 and MoS_2 Mono layer and Few-Layer Films," ACS Nano **9**, 7142-7150 (2015).
[174] D. Mao *et al.*, "WS_2 mode-locked ultrafast fiber laser," Scientific Reports **5**, 7965 (2015).
[175] P. Yan *et al.*, "Large-Area Tungsten Disulfide for Ultrafast Photonics," Nanoscale **9**, 1871-1877 (2017).
[176] C. Yin *et al.*, "Bright-Exciton Fine-Structure Splittings in Single Perovskite Nanocrystals," Physical Review Letters **119** (2017).
[177] Y. Cui, F. Lu and X. Liu, "Nonlinear Saturable and Polarization-induced Absorption of Rhenium Disulfide," Scientific Reports **7**, 40080 (2017).
[178] Y. Wang *et al.*, "Ultrafast recovery time and broadband saturable absorption properties of black phosphorus suspension," Applied Physics Letters **107**, 091905 (2015).
[179] D. Li *et al.*, "Polarization and Thickness Dependent Absorption Properties of Black Phosphorus: New Saturable Absorber for Ultrafast Pulse Generation," Scientific Reports **5**, 15899 (2015).
[180] W. Jie *et al.*, "Layer-Dependent Nonlinear Optical Properties and Stability of Non-Centrosymmetric Modification in Few-Layer GaSe Sheets," Angewandte Chemie International Edition **54**, 1185-1189 (2015).
[181] J. Sotor *et al.*, "Black phosphorus saturable absorber for ultrashort pulse generation," Applied Physics Letters **107**, 051108 (2015).
[182] G. H. Hu *et al.*, "Black phosphorus ink formulation for inkjet printing of optoelectronics and photonics," Nature Communications **8**, 278 (2017).
[183] W. D. Tan *et al.*, "Mode locking of ceramic Nd:yttrium aluminum garnet with graphene as a saturable absorber," Applied Physics Letters **96**, 031106 (2010).
[184] A. A. Lagatsky *et al.*, "2 μm solid-state laser mode-locked by single-layer graphene," Applied Physics Letters **102**, 013113 (2013).
[185] L. Li *et al.*, "High-power diode-side-pumped Nd:YAG solid laser mode-locked by CVD graphene," Optics Communications **315**, 204-207 (2014).
[186] L. Li *et al.*, "High repetition rate Q-switched radially polarized laser with a graphene-based output coupler," Applied Physics Letters **105**, 221103 (2014).
[187] R. Mary *et al.*, "1.5 GHz picosecond pulse generation from a monolithic waveguide laser with a graphene-film saturable output coupler," Optics Express **21**, 7943-7950 (2013).
[188] Z. P. Sun *et al.*, "A stable, wideband tunable, near transform-limited, graphene-mode-locked, ultrafast laser," Nano Research **3**, 653-660 (2010).
[189] D. Popa *et al.*, "Graphene Q-switched, tunable fiber laser," Applied Physics Letters **98**, 073106 (2011).
[190] Z. Sun *et al.*, "Ultrafast Stretched-Pulse Fiber Laser Mode-Locked by Carbon Nanotubes," Nano Research **3**, 404-411 (2010).
[191] D. Popa *et al.*, "Sub 200 fs pulse generation from a graphene mode-locked fiber laser," Applied Physics Letters **97**, 203106 (2010).
[192] T. Hasan *et al.*, "Solution-phase exfoliation of graphite for ultrafast photonics," Physica status solidi (b) **247**, 2953 (2010).
[193] M. Zhang *et al.*, "Tm-doped fiber laser mode-locked by graphene-polymer composite," Optics Express **20**, 25077-25084 (2012).

[194] C. A. Zaugg *et al.*, "Ultrafast and widely tuneable vertical-external-cavity surface-emitting laser, mode-locked by a graphene-integrated distributed Bragg reflector," Optics Express **21**, 31548-31559 (2013).
[195] T. Suhara and M. Fujimura. in *Waveguide Nonlinear-Optic Devices* 237-270 (Springer, 2003).
[196] T. J. Constant, S. M. Hornett, D. E. Chang and E. J. N. P. Hendry, "All-optical generation of surface plasmons in graphene," Nature Physics **12**, 124-127 (2016).
[197] C. Trovatello *et al.*, "Optical parametric amplification by monolayer transition metal dichalcogenides," Nature Photonics **15**, 6-10 (2021).
[198] A. Ciattoni, A. Marini, C. Rizza and C. Conti, "Phase-matching-free parametric oscillators based on two-dimensional semiconductors," Light: Science & Applications **7**, 5 (2018).
[199] R. W. Terhune, P. D. Maker and C. M. Savage, "Optical Harmonic Generation in Calcite," Physical Review Letters **8**, 404-406 (1962).
[200] B. C. Yao *et al.*, "Gate-tunable frequency combs in graphene-nitride microresonators," Nature **558**, 410-414 (2018).
[201] H. Chen *et al.*, "Enhanced second-harmonic generation from two-dimensional $MoSe_2$ on a silicon waveguide," Light: Science & Applications **6**, e17060 (2017).
[202] Y. Dai *et al.*, "Broadband Plasmon-Enhanced Four-Wave Mixing in Monolayer MoS_2," Nano Letters **21**, 6321-6327 (2021).
[203] N. Bernhardt *et al.*, "Quasi-BIC Resonant Enhancement of Second-Harmonic Generation in WS_2 Monolayers," Nano Letters **20**, 5309-5314 (2020).
[204] A. Autere *et al.*, "Nonlinear optics with 2D layered materials," Advanced Materials **30**, 1705963 (2018).
[205] S. S. Li *et al.*, "Vapour-liquid-solid growth of monolayer MoS_2 nanoribbons," Nature Materials **17**, 535-542 (2018).
[206] S. S. Li *et al.*, "Wafer-scale and deterministic patterned growth of monolayer MoS_2 via vapor-liquid-solid method," Nanoscale **11**, 16122-16129 (2019).
[207] H. Li *et al.*, "From Bulk to Monolayer MoS_2: Evolution of Raman Scattering," Advanced Functional Materials **22**, 1385-1390 (2012).
[208] H. Shi *et al.*, "Exciton dynamics in suspended monolayer and few-layer MoS_2 2D crystals," ACS Nano **7**, 1072-1080 (2013).
[209] F. Ceballos, Q. Cui, M. Z. Bellus and H. Zhao, "Exciton formation in monolayer transition metal dichalcogenides," Nanoscale **8**, 11681-11688 (2016).
[210] H. Wang, C. Zhang and F. Rana, "Ultrafast dynamics of defect-assisted electron-hole recombination in monolayer MoS_2," Nano Letters **15**, 339-345 (2015).
[211] Y. Li *et al.*, "Slow Cooling of High - Energy C Excitons Is Limited by Intervalley - Transfer in Monolayer MoS_2," Laser & Photonics Reviews **13** (2019).
[212] T. Goswami, R. Rani, K. S. Hazra and H. N. Ghosh, "Ultrafast Carrier Dynamics of the Exciton and Trion in MoS_2 Monolayers Followed by Dissociation Dynamics in Au@MoS_2 2D Heterointerfaces," The Journal of Physical Chemistry Letters **10**, 3057-3063 (2019).
[213] Z. Nie *et al.*, "Ultrafast Carrier Thermalization and Cooling Dynamics in Few-Layer MoS_2," ACS Nano **8**, 10931-10940 (2014).
[214] M. Kourogi, K. i. Nakagawa and M. Ohtsu, "Wide-span optical frequency comb generator for accurate optical frequency difference measurement," IEEE Journal of Quantum Electronics **29**, 2693-2701 (1993).
[215] W. A. T. III, "Hot Electron Dynamics at Semiconductor Surfaces: Implications for Quantum Dot Photovoltaics," thesis (2010).
[216] J. Cheng *et al.*, "Chiral selection rules for multi-photon processes in two-dimensional honeycomb materials," Optics letters **44**, 2141-2144 (2019).
[217] R. D. Schaller, J. C. Johnson and R. J. Saykally, "Time-resolved second harmonic generation near-field scanning optical microscopy," Chemphyschem **4**, 1243-1247 (2003).
[218] D. Bodlaki and E. Borguet, "Dynamics and second-order nonlinear optical susceptibility of photoexcited carriers at Si(111) interfaces," Applied Physics Letters **83**, 2357-2359 (2003).
[219] E. M. Mannebach *et al.*, "Ultrafast electronic and structural response of monolayer MoS_2 under intense photoexcitation conditions," ACS Nano **8**, 10734-10742 (2014).
[220] S. P. Rodrigues and W. Cai, "Nonlinear optics: Tuning harmonics with excitons," Nature Nanotechnology **10**, 387-388 (2015).

[221] H. Jang *et al.*, "Transient SHG imaging on ultrafast carrier dynamics of MoS_2 nanosheets," Advanced Materials **30**, e1705190 (2018).
[222] K. P. Dhakal *et al.*, "Probing the upper band gap of atomic rhenium disulfide layers," Light: Science & Applications **7**, 98 (2018).
[223] M. Taghinejad *et al.*, "Photocarrier-induced active control of second-order optical nonlinearity in monolayer MoS_2," Small, e1906347 (2020).
[224] M. Taghinejad *et al.*, "Transient Second-Order Nonlinear Media: Breaking the Spatial Symmetry in the Time Domain via Hot-Electron Transfer," Physics Review Letters **124**, 013901 (2020).
[225] S. Cha *et al.*, "1s-intraexcitonic dynamics in monolayer MoS_2 probed by ultrafast mid-infrared spectroscopy," Nature Communications **7**, 10768 (2016).
[226] J. Xiao *et al.*, "Nonlinear optical selection rule based on valley-exciton locking in monolayer WS_2," Light: Science & Applications **4**, e366 (2015).
[227] L. Alloatti *et al.*, "100 GHz silicon–organic hybrid modulator," Light: Science & Applications **3**, e173-e173 (2014).
[228] Y. Wang *et al.*, "Giant All-Optical Modulation of Second-Harmonic Generation Mediated by Dark Excitons," ACS Photonics **8**, 2320-2328 (2021).
[229] B. Zhu, X. Chen and X. Cui, "Exciton binding energy of monolayer WS_2," Scientific Reports **5**, 9218 (2015).
[230] A. Autere *et al.*, "Optical harmonic generation in monolayer group-VI transition metal dichalcogenides," Physical Review B **98**, 115426 (2018).
[231] W. Li *et al.*, "Broadband optical properties of large-area monolayer CVD molybdenum disulfide," Physical Review B **90**, 195434 (2014).
[232] A. Chernikov *et al.*, "Exciton binding energy and nonhydrogenic Rydberg series in monolayer WS_2," Physics Review Letters **113**, 076802 (2014).
[233] Y. Cheng *et al.*, "Ultrafast Optical Modulation of Harmonic Generation in Two-Dimensional Materials," Nano Letters **20**, 8053-8058 (2020).
[234] F. Ceballos and H. Zhao, "Ultrafast Laser Spectroscopy of Two-Dimensional Materials Beyond Graphene," Advanced Functional Materials **27**, 1604509 (2017).
[235] Z. Chi *et al.*, "Ultrafast Energy Dissipation via Coupling with Internal and External Phonons in Two-Dimensional MoS_2," ACS Nano **12**, 8961-8969 (2018).
[236] M. Palummo, M. Bernardi and J. C. Grossman, "Exciton radiative lifetimes in two-dimensional transition metal dichalcogenides," Nano Letters **15**, 2794-2800 (2015).
[237] L. Yuan *et al.*, "Exciton Dynamics, Transport, and Annihilation in Atomically Thin Two-Dimensional Semiconductors," The Journal of Physical Chemistry Letters **8**, 3371-3379 (2017).
[238] Z. E. Eroglu *et al.*, "Ultrafast dynamics of exciton formation and decay in two-dimensional tungsten disulfide (2D-WS_2) monolayers," Physical Chemistry Chemical Physics **22**, 17385-17393 (2020).
[239] T. Yan *et al.*, "Probing the exciton k-space dynamics in monolayer tungsten diselenides," 2D Materials **6**, 025035 (2019).
[240] K. Tran *et al.*, "Evidence for moire excitons in van der Waals heterostructures," Nature **567**, 71-75 (2019).
[241] C. Jin *et al.*, "Observation of moire excitons in WSe_2/WS_2 heterostructure superlattices," Nature **567**, 76-80 (2019).
[242] N. H. Burnett, H. A. Baldis, M. C. Richardson and G. D. Enright, "Harmonic generation in CO_2 laser target interaction," Applied Physics Letters **31**, 172-174 (1977).
[243] T. T. Luu *et al.*, "Extreme ultraviolet high-harmonic spectroscopy of solids," Nature **521**, 498-502 (2015).
[244] H. Kim *et al.*, "Generation of Coherent Extreme-Ultraviolet Radiation from Bulk Sapphire Crystal," ACS Photonics **4**, 1627-1632 (2017).
[245] O. Schubert *et al.*, "Sub-cycle control of terahertz high-harmonic generation by dynamical Bloch oscillations," Nature Photonics **8**, 119-123 (2014).
[246] Z. Y. Lou *et al.*, "Ellipticity dependence of nonperturbative harmonic generation in few-layer MoS_2," Optics Communications **469**, 125769 (2020).
[247] N. Klemke *et al.*, "Polarization-state-resolved high-harmonic spectroscopy of solids," Nature Communications **10**, 1319 (2019).
[248] Y. Bai *et al.*, "High-harmonic generation from topological surface states," Nature Physics **17**, 311 (2020).
[249] J. D. Cox, A. Marini and F. J. de Abajo, "Plasmon-assisted high-harmonic generation in graphene," Nature Communications **8**, 14380 (2017).

[250] F. Langer *et al.*, "Lightwave valleytronics in a monolayer of tungsten diselenide," Nature **557**, 76-80 (2018).
[251] T. Higuchi *et al.*, "Light-field-driven currents in graphene," Nature **550**, 224-228 (2017).
[252] A. Chaves *et al.*, "Bandgap engineering of two-dimensional semiconductor materials," npj 2D Materials and Applications **4**, 1-21 (2020).
[253] Y. Cao *et al.*, "Unconventional superconductivity in magic-angle graphene superlattices," Nature **556**, 43-50 (2018).
[254] E. M. Alexeev *et al.*, "Resonantly hybridized excitons in moire superlattices in van der Waals heterostructures," Nature **567**, 81-86 (2019).
[255] K. L. Seyler *et al.*, "Signatures of moire-trapped valley excitons in $MoSe_2/WSe_2$ heterobilayers," Nature **567**, 66-70 (2019).
[256] N. Leisgang *et al.*, "Giant Stark splitting of an exciton in bilayer MoS_2," Nature Nanotechnology **15**, 901-907 (2020).
[257] I. C. Gerber *et al.*, "Interlayer excitons in bilayer MoS_2 with strong oscillator strength up to room temperature," Physical Review B **99**, 035443 (2019).
[258] Y. Shan *et al.*, "Stacking symmetry governed second harmonic generation in graphene trilayers," science advanced **4**, eaat0074 (2018).
[259] F. Yang *et al.*, "Tunable Second Harmonic Generation in Twisted Bilayer Graphene," Matter **3**, 1361-1376 (2020).

Since the first reported second-harmonic generation (SHG) in 1961, harmonic generations (HGs) play an increasingly important role in various technologies, especially in our modern information society. However, nonlinear optical effects normally have relatively low efficiency to be controlled. Therefore, reinforcing and controlling the efficiency of HGs are of importance for numerous applications of nonlinear optics.

Thanks to the recent discovery and development of two-dimensional (2D) materials with excellent physical properties, this thesis studies the transient linear and nonlinear optical processes in 2D materials, offering a way to control and enhance nonlinear optical responses in nanoscale. Our results have revealed that 2D materials are promising for actively engineered nonlinear optics in nanophotonics and nanoelectronics.

Aalto-DT 31/2022

ISBN 978-952-64-0714-2 (printed)
ISBN 978-952-64-0715-9 (pdf)
ISSN 1799-4934 (printed)
ISSN 1799-4942 (pdf)

Aalto University
School of Electrical Engineering
Department of Electronics and Nanoengineering
www.aalto.fi

BUSINESS + ECONOMY

ART + DESIGN + ARCHITECTURE

SCIENCE + TECHNOLOGY

CROSSOVER

DOCTORAL THESES